UNIVERSITY OF THE
WITWATERSRAND,
JOHANNESBURG

MODELLING OF GAS RECOVERY FROM SOUTH AFRICAN SHALE RESERVOIRS (Focusing on the KWV-1 Bore hole in the Eastern Cape Province)

Prepared by

Nkhabu Robert Makoloane

(536698)

A research report submitted to the Faculty of Engineering and Built Environment, University of the Witwatersrand, Johannesburg, South Africa, in partial fulfilment of the requirements for the Degree of Master of Science in Engineering.

Supervisor: Dr. DB Nkazi

November, 2018

Declaration

I, Nkhabu Robert Makoloane (Student Number: 536698) am a student registered for *Master of Science in Engineering* (Chemical) in the year 2018. I hereby declare the following:

- I am aware that plagiarism (the use of someone else's work without their permission and/or without acknowledging the original source) is wrong.
- I confirm that the work submitted for assessment for the above course is my own unaided work except where I have explicitly indicated otherwise.
- I have followed the required conventions in referencing the thoughts and ideas of others.
- I understand that the University of the Witwatersrand may take disciplinary action against me if there is a belief that this is not my own unaided work or that I have failed to acknowledge the source of the ideas or words in my writing.

Signature: ____________________ Date: November 26, 2018

Dedication

In memory of my late father

Lehana Mokhu Benny Nkhabu.

Acknowledgements

I would like to thank the Almighty God the Father, Son the king of Heaven and the Holy Spirit the comforter, for guiding me in this project.

It gives me a great pleasure to share my gratitude to my supervisor Dr DB Nkazi, he is a busy person, but the guidance he gave in this project was marvellous. Thanks go to my colleagues at ArcelorMittal Vanderbijlpark (Coke Making) who covered for me when I was away preparing for my final submission of the report. I would also like to acknowledge my Supervisor at work for allowing me to take some time off to prepare for the submission of this report and special mention to Joyful Mdlhuli for the support.

To Katlego Phanyane thank you for helping me in editing this project and the advice you shared with regards to the structure of an engineering report. Thanks to my family for being patient with me when I couldn’t be there on the dining table.

Many thanks go to my mother (Makopano Nkhabu Qefate) who continuously pray for me and who motivated me to undertake this study.

.

Abstract

The main aim of the study was to develop mathematical flow model of the shale gas at the Karoo Basin of South Africa (SA). The model development incorporates three systems (phases) to form a triple continuum flow model, the phases include matrix (*m*), natural (NF) and hydraulic fracture (HF).

The model was developed from the continuity equation, and the general equations were formed.

$$(0.05\frac{\partial p_m}{\partial t} = 3.90087\times10^{-15}\frac{\partial^2 p_m}{\partial x^2} + 3.90087\times10^{-15}\frac{\partial^2 p_m}{\partial x^2} - 1.95043\times10^{-16}(20\times10^6 - p_{NF}),$$

$$0.01\frac{\partial p_{NF}}{\partial t} = 2.00\times10^{-15}(20\times10^6 - p_{NF}) - 2.00\times10^{-9}(20\times10^6 - p_{HF}) + \frac{\partial}{\partial x}\left[7.80\times10^{-5}\frac{\partial p_{NF}}{\partial x}\right] + \frac{\partial}{\partial y}\left[7.80\times10^{-5}\frac{\partial p_{NF}}{\partial y}\right]$$

$$\frac{\partial}{\partial y}\left[0.1248269\frac{\partial p_{HF}}{\partial y}\right] + 0.1248269(20\times10^6 - p_{HF}) - 4.98\times10^{-4} = \frac{\partial p_{HF}}{\partial t}$$

The model was solved using numerical method technique known as Finite Difference Method (FDM). For each phase a computer program MATLAB was used to plot the pressure gradient. Hydraulic pressure gradient fractures propagate between the distance of 100m and 500m. The model was verified using the data of Barnett Shale. Sensitivity analysis was also performed on the hydraulic permeability, drainage radius and the initial pressure of the reservoir.

Contents

List of Figures

List of Tables

Nomenclature

Item	Units	Symbol
Natural fracture		NF
Hydraulic fracture		HF
Matrix to natural fractures		mNF
Reservoir thickness	m	h
Reservoir length,	m	
Reservoir breadth	m	
Effective thickness	m	
Fracture half-length	m	
Interface area		A
Klinkenberg coefficient	MPa	b
Klinkenberg coefficient (NF)	MPa	b_{NF}
Klinkenberg coefficient (m)	MPa	b_m
Matrix porosity,		ϕ_m
Natural fracture porosity,		ϕ_{NF}
Hydraulic fracture porosity,		ϕ_{HF}
Skin Factor		S
Compressibility factor,		Z
Normal direction		n
Fracture spacing	m	
Wellbore radius,	m	r_w
Initial reservoir pressure	Pa	p_i
Bottom-hole pressure	Pa	p_w
Langmuir pressure	Pa	p_L
Matrix pressure	Pa	p_m
Natural fracture pressure	Pa	p_{NF}
Hydraulic fracture pressure	Pa	p_{HF}
Langmuir pressure	Pa	p_L
Mass flux of the adsorbed gas	[kg/(m^3 s)]	q_{ad}
Inter-porosity flow from matrix to natural fracture	[kg/(m^3 s)]	q_m
Inter-porosity flow from natural fracture to hydraulic fracture	[kg/(m^3 s)]	q_{NF}
Reservoir temperature	K	T
Langmuir volume,	cm^3/ cm^3	V_L
Apparent permeability	m^2	k_a
Absolute permeability	m^2	k_i
Absolute permeability of matrix	m^2	k_{mi}
Apparent permeability of matrix	m^2	k_{ma}
Absolute permeability of natural fracture	m^2	k_{NFi}
Apparent permeability of natural fracture	m^2	k_{NFa}
Permeability of hydraulic fracture	m^2	k_{HF}

Molecular weight of gas	kg/mol	M_g
Interface area per unit volume of rock	m^{-1}	$A_{m\rightarrow NF}$
Interface area per unit volume of rock	m^{-1}	$A_{NF\rightarrow HF}$
NF Characteristic length	M	L_{NF}
HF Characteristic length	M	L_{HF}
Gas Viscosity	cP	μ_g
Gas compressibility	MPa^{-1}	C_g
Flow term from HF to the horizontal to the horizontal well	[kg/(m3 s)]	q_w
Gas rate (Gas production)	m3/day	q
Cumulative gas production		Q
Universal gas constant	[Pa m^3/(kmol K)]	R
Length in direction parallel to the horizontal well	M	x
Effective radius of the grid where HF intersects with wellbore	M	r_e
Matrix to natural fracture		mN
Natural fracture to hydraulic fracture		NH
Length in direction perpendicular to the horizontal well	M	y
Gas density	(kg/m^3)	
Reservoir boundary		
Inter-porosity flow shape factor (m)		a
Time	(s)	t
Volume of a specific grid	(m^3)	$V_{i,j}$
Langmuir volume	(m^3/m^3)	V_L
Adsorbed gas content	(m^3/m^3)	V_E

CHAPTER 1 INTRODUCTION

More research on the recovery of shale reservoirs (unconventional oil and gas source) is necessary in this lifetime; the motivation is brought by the gradual declining sources of conventional reservoirs and high energy demand from global community. Gas production from shale in the United States of America (USA) and the United Kingdom (UK) has contributed to the increasing interest in recovering this volatile form of energy. It is becoming an important form of energy to the rest of the world because it bridges the gap between demands and supply of the world's energy (De Wit, 2011). The USA has an annual natural gas production in the form of shale gas estimated to be 1.0 trillion of standard cubic feet (TSCF) from 40 000 wells (Renyi et al., 2017).

Technological improvements in horizontal well drilling to recover tight gas and shale gas have shifted the attention of researchers on recovery of this gas/oil trapped in the source sedimentary rocks (unconventional sources). Confinement in the form of fine small interstitial space and low penetration of grained sedimentary rock is defeated by level penetration and hydraulic fracking (Kudapa et al., 2017). For continued success in exploring and exploiting the unconventional reservoirs, this research focuses on the shale gas recovery from the Karoo region in South Africa (SA).

1.1 Overview of local shale gas production and consumption

SA has a declining rate of conventional production of natural gas which is largely produced from the offshore areas. Referring to Figure1.1, in 2007 the production of approximately 100 billion cubic feet (BCF) was the highest between period 2005 to 2010, and also within the same period the consumption was highest at about 200 BCF. The shortfall was covered through importation from Mozambique.

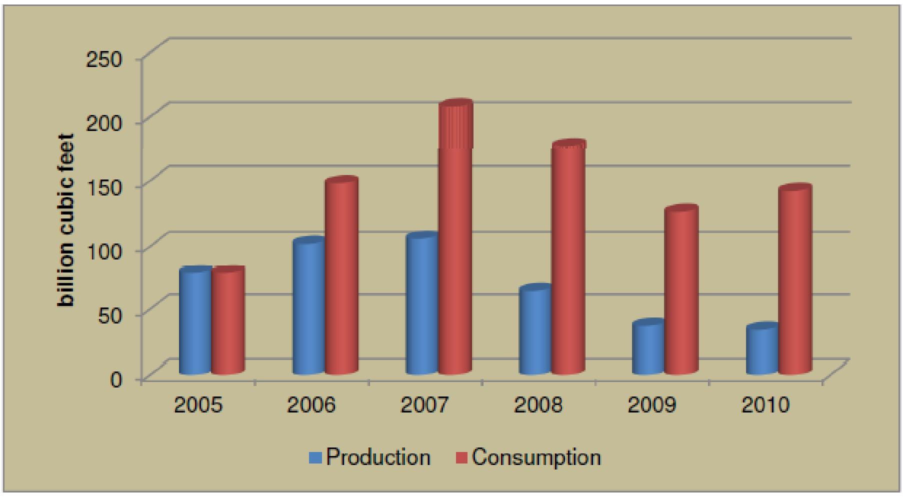

Figure 1.1 SA natural gas production and consumption (SAMSA, 2011)

From 2008, the production has been declining significantly and consumption has been greater than the production, the difference between consumption and production has been covered through import as explained above. In general, Figure 1.1 shows that natural gas demand is greater than the country's production since 2006 to 2010. Therefore, it is necessary for SA to recover shale gas. Gas is cheaper to produce and has a comparatively low carbon footprint compared to coal and oil (Bo et al., 2017). Another benefit for producing shale gas is that it can also be used in the industry and domestically for heating which will then decrease the high rate of imports of oil and gas.

Modelling of gas production is not a new subject in the petroleum industry. The current knowledge gives a general approach to it, so to accommodate the South African land scape, it is therefore fitting to model and simulate the gas shale production for SA's reservoirs. Industrial application will be for fracking in the Karoo to recover an estimated13-211 trillion cube feet (TCF) reserves of shale gas (De Kock et al., 2017). This is according to the carbonaceous shale thickness, depth, area, heat maturity as well as the total organic compounds (TOC) as determined on the Ecca Group's Whitehill, (refer to Figure 1.2) (De Kock et al., 2017).

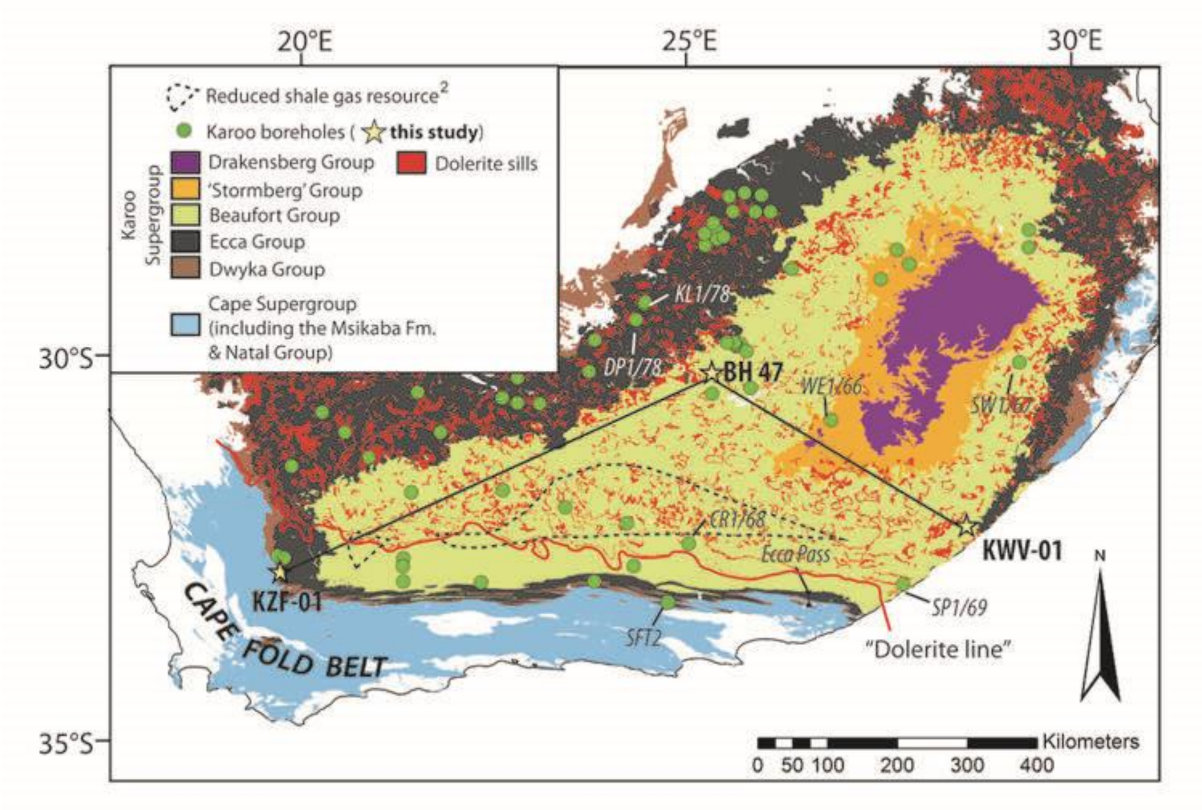

Figure 1.2 The main Karoo Basin showing the position of the three drills cores for the study by the South African Geologist (De Kock et al., 2017)

The study divulged a down grade of reserves estimated from 485 TCF to 13 TCF (De Kock et al., 2017).

1.2 The economics of the shale gas

The economics of the shale gas recovery is depended mainly on the actual gas that can be recovered in comparison to the original gas in place (OGIP) estimation (Cooper et al., 2016). The total actual gas recovery rate is dependent on the technology, reservoir design, fracture creation and geology knowledge (functions) (Saliem, 2015). Combination of these functions to the total actual gas recovery is beneficial to make sure production costs, and operation costs are reduced overtime.

In later years professional specialists have analysed production data from different reservoirs, and it can be concluded that the producing reservoirs follow a fairly well known general pattern (Tan et al., 2018). Shale gas production in the first 2-3 years shows high decline rates of production and as years pass by it balances off, meaning that the decline rates are not as aggressive as the first 2-3 years of production. Referring to the Figure 1.3, decline rates of shale gas reservoir is more significant than the conventional reservoir. Shale gas reservoir differs significantly with conventional reservoir because of the steep. Shale gas's initial production (IP) and decline rates influence economic limit and profitability.

The trajectory of Figure 1.3 is influenced by geophysical and petro physical characteristics of the reservoirs, since it is at this stage where gas production profile moves from free gas to adsorbed gas. Also occurring is the production profile dominated by fractures then changes to production dominated by the rock matrix.

Arp's formula has been used since 1945 to estimate the amount of oil or gas that can be produced and also to estimate as to when production can come to an end for the conventional reservoir. Recently the formula has also been used, however modifications on the formula are still on going to improve accuracy in the way it estimates production of the shale reservoir.

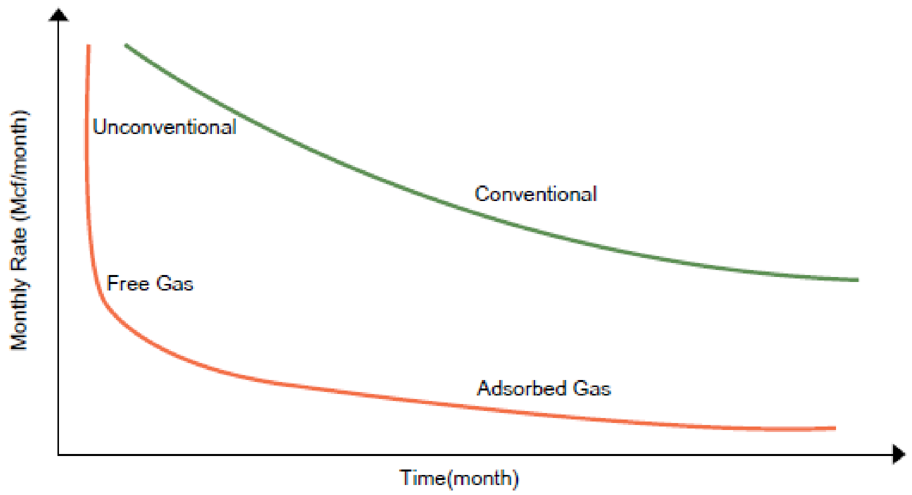

Figure 1.3 Decline curves of conventional against unconventional reservoir (Saliem, 2015)

1.3 The aim and objectives

The main aim of the study is to mathematically model the flow of the shale gas at the southern Main Karoo Basin of SA (KWV-1). The flow model will be the incorporation of three systems to form a triple continuum flow model. The system will include matrix known for very low permeability, natural fracture with low permeability and hydraulic fracture with high permeability.

Accordingly, the following objectives are to be undertaken:

- Establish triple porosity model for the general shale gas reservoir using data that is currently available from literature.
- Validate the model by using field data and simulation from (Guo, et al., 2018)'s literature, which is of multistage horizontal well fracturing.
- Investigate the effect of changing the permeability of hydraulic fracture against the production rate.
- Investigate the effect of changing the external radius (r_e) on the production rate.
- Investigate the effect of changing the initial pressure ($p_m = p_{NF} = p_{HF} = p_i$) against the production rate.

CHAPTER 2 LITERATURE REVIEW

Many articles have been published concerning the modelling of gas production from unconventional resources (Wang et al., 2015). The unconventional oil and gas reservoirs have challenges which are in the form of low permeability from the source rock which is not a major problem from the traditional conventional oil and gas. Unconventional gas reservoirs usually consists of coal bed methane, gas pressurized zones, tight gas sands together with deep shale gas (Correa et al., 2009). The study will focus mainly on shale gas in South African context. The bore-hole KWV-1 properties will be used to demonstrate the properties of the main Southern Karoo.

2.1 Shale reservoir characteristics-Karoo Basin

Shale rocks are an unconventional energy source which contains Kerogen, of which is a chemical compound that is converted into useful hydrocarbons by pyrolysis (Speight, 2008). The sedimentary rocks make up the shale formations which are grouped as mudstones and clay. One of the resource assessments was conducted by Geel et al., (2013) on the Karoo sedimentary rock deposition. The dropstone was found to lie at the bottom of the Ecca group, which is also known as the Prince Albert Formation. The Prince Albert Formation is made up of the mudstone, shale and small units of sandstone.

The Whitehill Formation is characterised as the fine-grained, well-laminated black organic rich shale which is weathered because of oxidation reactions taking place on the hydrated calcium sulphate (Johnson et al., 1996). This is the formation that is more important due to it being able to break down to form gas and oil. The Collingham Formation constitutes of very dark grey mudstones, inserted between layers with yellowish layers of ash fall which is dated 274-270 Ma (Viljoen 1994, Geel et al. 2013). Generally, mudstones are parallel laminate, they can undergo nuclear fission and they also contain fossil traces like Planolites (Geel et al., 2013).

2.2 Shale gas recovery mechanisms

Shale gas is categorised as unconventional gas, and it is associated with sources such as shale rock, sand stones and coal seams which possess low porous and permeability characteristics (Guarnone et al., 2012). To extract shale gas economically, two technologies are deployed namely horizontal drilling and hydraulic fracturing.

2.2.1 Horizontal drilling

Horizontal drilling begins with a vertical shaft being drilled vertically downwards until it hits just above the targeted gas/oil reservoir. It then re-orientates and turns into a direction that will make its path horizontal, see Figure 2.1 its horizontal path will continue until the required length is achieved. Horizontal drilling increases the production rate of the well due to its increased contact with the productive layer of the well (Chaoa et al., 2016). According to (Burwen and Flegal, 2013) initial costs of the directional reservoir construction is two to three times the cost of conventional recovery of the gas. However the initial production is three to four times greater than that of the conventional reservoir (Burwen and Flegal, 2013).

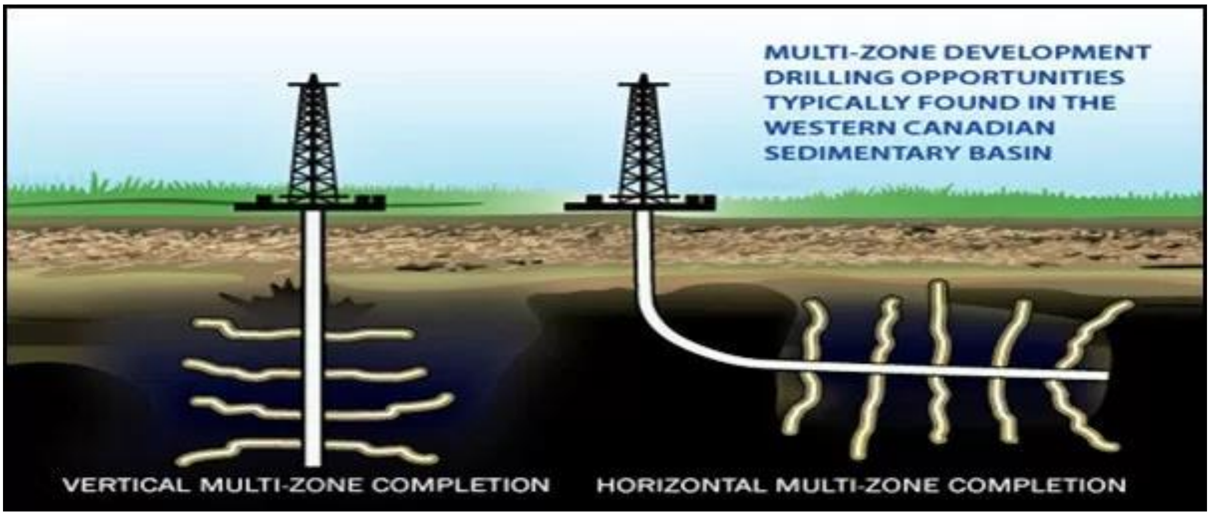

Figure 2.1 Vertical and horizontal drilling (Anon., 2018)

2.2.2 Hydraulic fracturing

Hydraulic fracturing (HF) famously known as fracking, is a process of stimulating the shale rock and sand stones with a mixture of high pressured liquid (Belyadi et al., 2017). This liquid is a mixture of water, proppant, and chemicals injected at high pressure into a well bored. The gradual accumulation of the pressure causes the formation to crack through where the proppant keeps cracks open to allow the free flow of natural gas to the well where it will be extracted (Belyadi et al., 2017). Overtime the cracks self-seal due to natural occurrence, hence it requires fracturing repeatedly. HF takes place after drilling and it is shown in Figure 2.2 as horizontal cracking takes place.

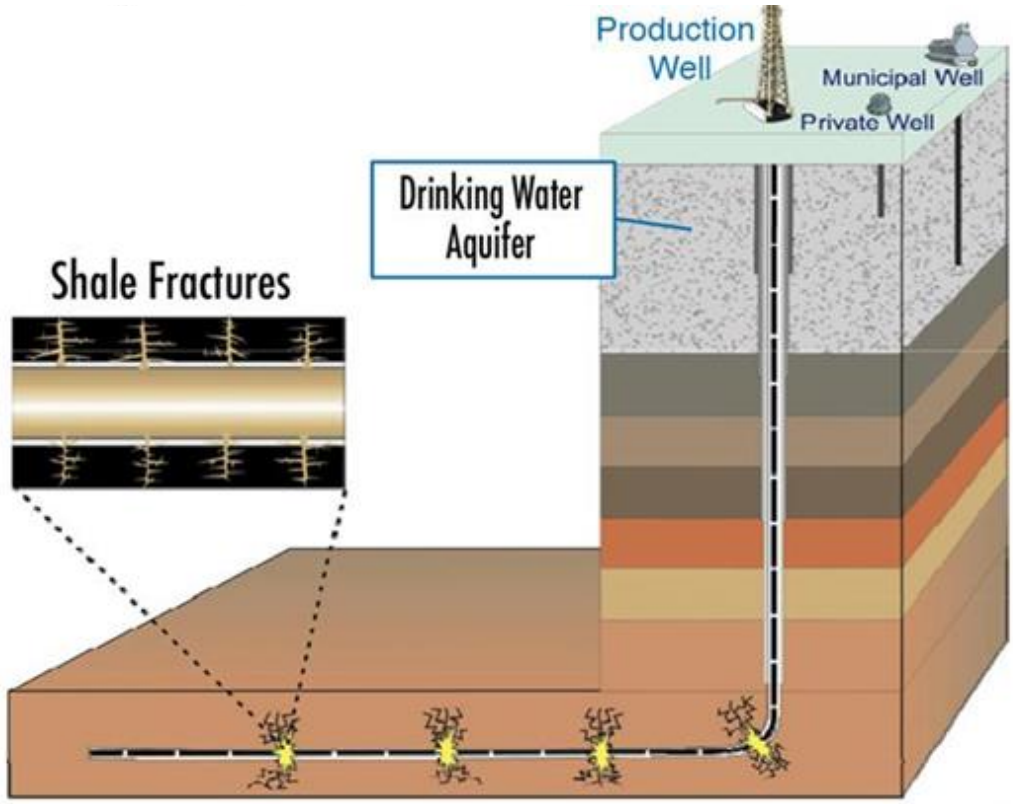

Figure 2.2 Hydraulic fracturing process following drilling of the well (Degenhardt, 2011)

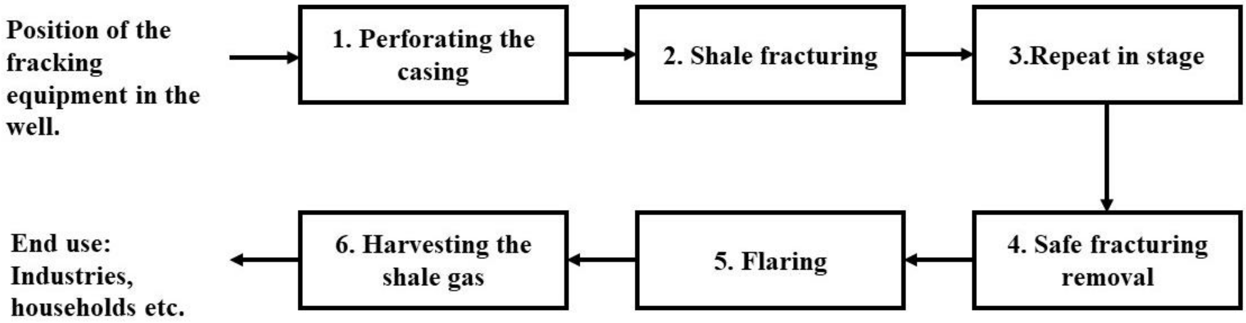

Figure 2.3 Hydraulic fracturing block flow diagram (Ahmed, 2001)

Hydraulic Fracturing Process referring to Figure 2.3

Stage 1: Lowering of the perforating equipment into a target area within the horizontal portion of the well. The electric charge is travelled down the well to initiate a small explosive charge.

Stage 2: Creating a network of cracks in the shade rock pumping the fracking fluid.

Stage 3: Experts monitor the process parameters in each stage to ensure safe operation, public safety and maximise natural gas product.

Stage 4: Drilling out the plugs to remove the restriction in the wellbore, this is to allow the collection of gas. The collected fracturing fluid is treated and reused again in the process.

Stage 5: Towards completion of removing the fracturing fluid, the gas which is moving up the well with the fracturing fluid has greater volume than the fracturing fluid. In order not to cause fire, flaring takes place as a safety precaution.

Stage 6: When the process of removing the fracturing fluid is complete, sand remains which creates a passage way into the wellbore and eventually to the earth’s surface.

Stage 7: End user, businesses, household, industries.

2.3 Gas flow patterns and characterisation of fluid flow through the porous media.

Hydraulically fractured well flow pattern is influenced by reservoir geometry (Ahmed, 2001). In most reservoirs their shapes have irregular boundaries, hence authorises use of rigorous mathematical analysis. There are 5 well defined flow patterns in hydraulically fractured well, which are depicted in Figure 2.4; (a) fracture linear, (b) bilinear, (c) formation linear, (d) elliptical and (e) pseudo radial flow pattern. The first 3 patterns can be grouped as fracture linear.

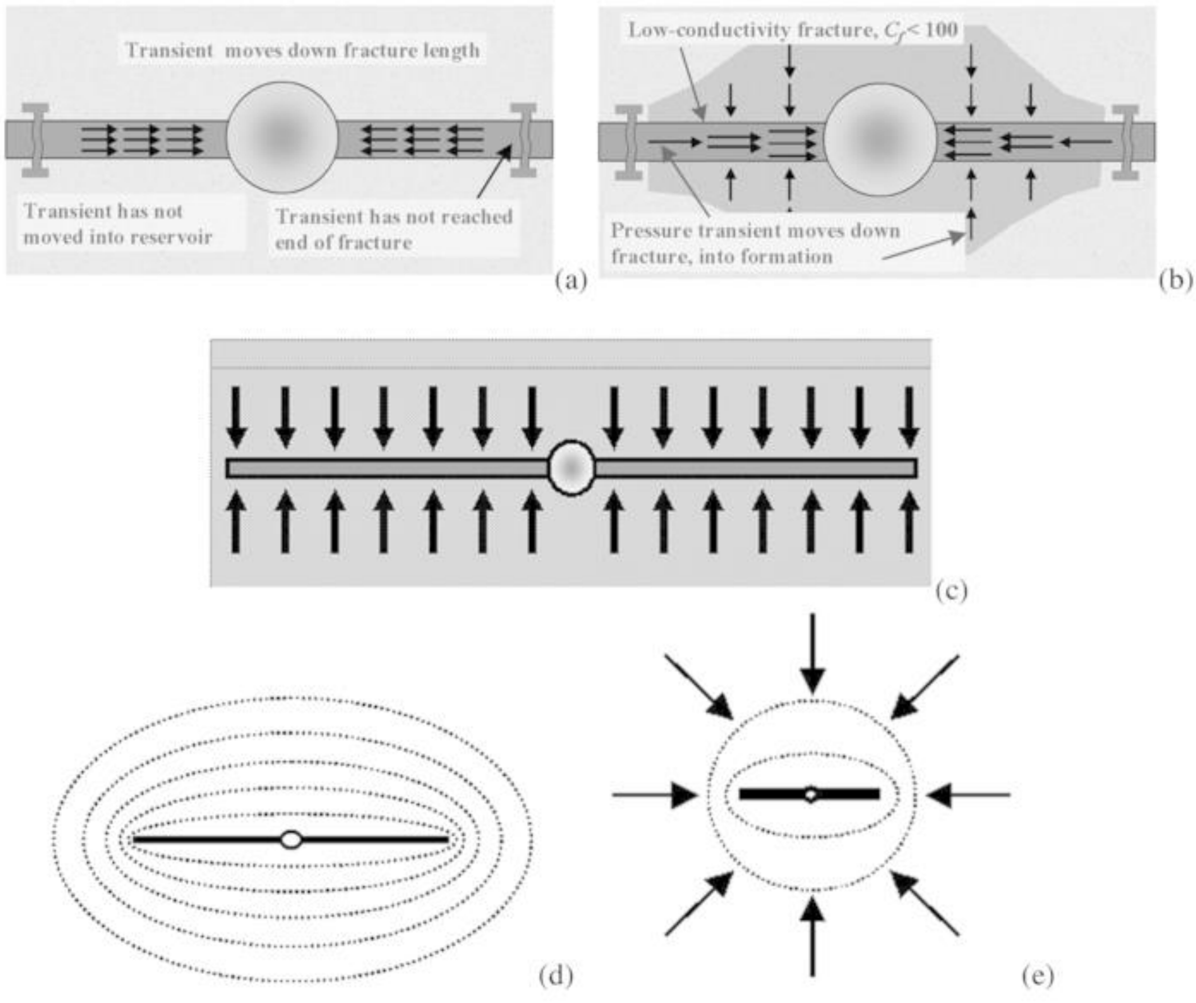

Figure 2.4 Flow patterns for the hydraulically fractured well. ; (a) fracture linear, (b) bilinear, (c) formation linear, (d) elliptical and (e) pseudo radial flow pattern (Cinco-Ley and Samaniego-V., 1981)

Fracture linear: Is a fluid flow regime that exists because of a hydraulically fractured well. Its purpose is to examine methodically facts and statistics collected to determine the fracture half-length. This flow regime does not last long and is often hidden by effects of the well (Cinco-Ley and Samaniego-V., 1981).

Elliptical flow regime: Is the transitional fluid flow between linear flows and pseudo radial flow. This flow pattern takes place the moment the fluid has begun to move from the reservoir at one end of the horizontal well bore.

Pseudo Radial flow pattern: Radial fluid flows into or away from a wellbore in absence of the reservoir, heterogeneity is assumed to be a cylindrical flow across the formation on the horizontal (Ahmed, 2001). The fluid flows radically towards the well bore, this assumed radial flow characterises the flow of fluid into the wellbore.

2.4 Modelling Darcy and Non-Darcy flow in hydraulic fractures

2.4.1 Darcy flow

Darcy's law (equation 2.1) describes the flow of fluid in a porous medium, according to (Basniev et al., 2012) this law has an empirical relationship which focuses on experimental observations that comprised of water flow in one dimension through packed sand at low velocity. With reference to equation 2.1, the pressure gradient is linearly proportional to the fluid velocity in the porous media.

$$\frac{-dp}{dx} = \frac{\mu v}{k} \tag{2.1}$$

Where p is the pressure, x the direction of fluid flow, μ is the viscosity, v the superficial velocity and k is the permeability.

2.4.2 Non-Darcy Flow

Non-Darcy flow (law) significantly outlines the fluid flow in a porous media whereby there is a high flow rate and Reynold's number of gas near the well (Zeng and Grigg, 2006). This region is in between laminar flow and turbulent flow and eventually transits to the turbulent flow. The effect of non-Darcy is a rate-dependent skin effect, 40 years later after Darcy's law was recognised; Forchheimer observed that as the gas velocity increases, Darcy's law doesn't hold anymore (Crain, 2006). Meaning that it becomes nonlinear as illustrated below by Figure 2.5 For instance, inside the hydraulic fractures there are significant effects of the inertia that occur, which then causes further pressure difference to drop in the hydraulic fracture to maintain the production rate.

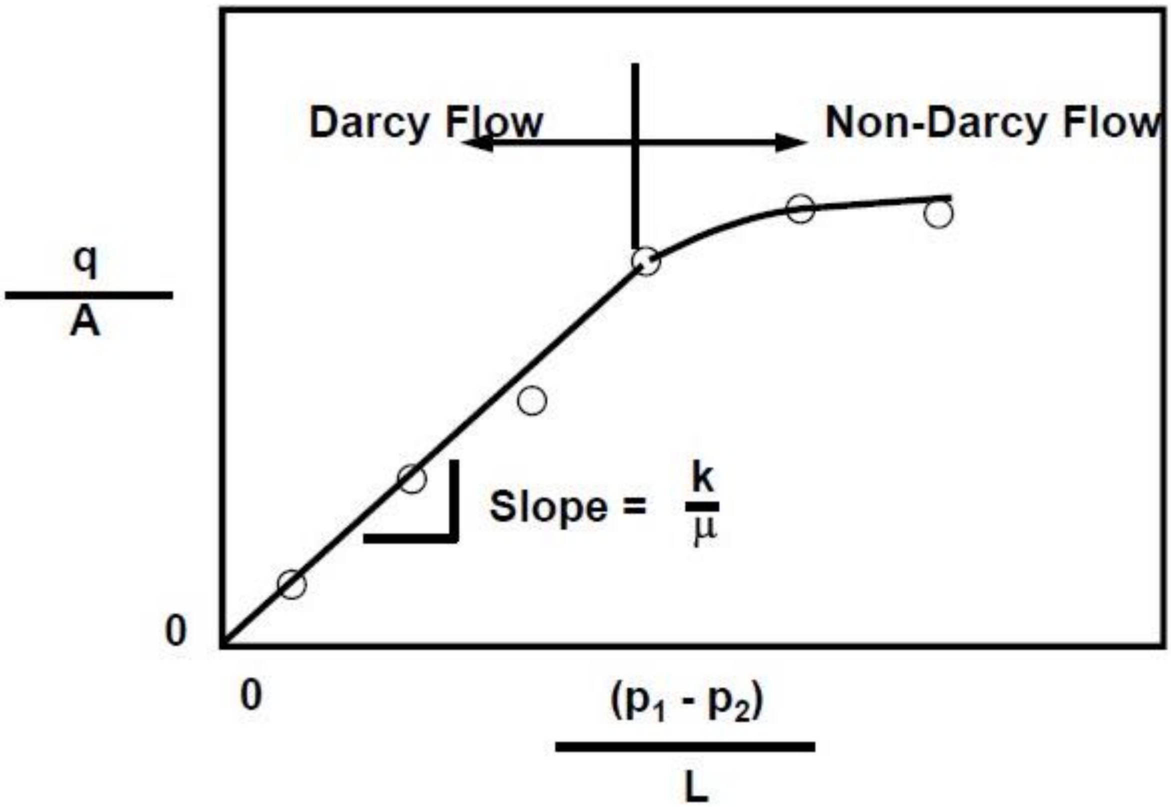

Figure 2.5 Non-Darcy' law velocity against pressure gradient (Crain, 2006)

In mathematical terms this was explained by Forchheimer by introducing the second constant (β) into Darcy's law and is illustrated as equation (2.2) (Crain, 2006):

$$\frac{-dp}{dx} = \frac{\mu v}{k} + \beta \rho v^2 \tag{2.1}$$

Where β is the non-Darcy flow coefficient.

2.5 Basic Reservoir Model Simulation

In accordance with the spatial scale flow of gas in the shale formation it is expected to yield many different mechanisms. Natural fracture and hydraulic fracture depict huge dissimilarity for conductivity and connectivity. Hence, dual porosity which mainly focuses on the simulation of fluid flow for naturally fractured reservoirs and triple porosity model which focuses on the simulation of shale gas with complicated shale gas flow and production will be explored.

2.5.1 Dual-porosity model

Dual porosity is mostly used when simulating fluid flow for naturally fractured reservoirs. Fundamental use of this model was brought forward by (Barenblatt et al., 1960). The model was modified by (Warren & Root, 1963) and it was introduced into petroleum literature for the well testing analysis. The modified model governed the matrix-fracture flow; the matrix block as seen in Figure 2.6 has high porosity and low permeability (Guo et al., 2018). The fracture criss-cross has low porosity and high conductivity. The model is grouped into two: pseudo steady-state and unsteady state.

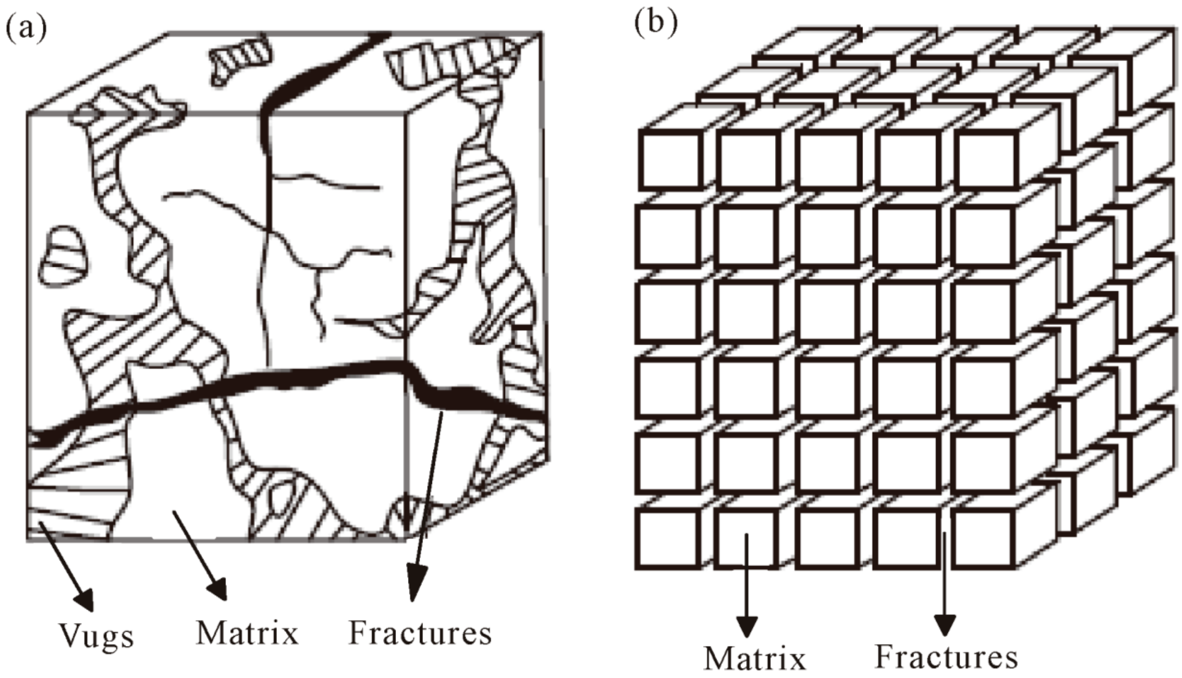

Figure 2.6 Dual porosity model (a) actual reservoir (b) grid model (Warren and Root, 1963)

Pseudo steady state refers to when the flow is between the matrix and fracture system, meaning that the pressure at the matrix grid is becoming different at time is equal to zero.

The mathematical terms of the two diffusion equations; one from the matrix and the other from fracture are solved simultaneously resulting equation (2.3) of transfer rate term:

$$q_m = \frac{\rho_g k_{ma} \alpha_{m-NF} (p_m - p_{NF})}{\mu_g} \qquad (2.3)$$

Where q_m is the transfer rate, $\rho_g$is the density of gas, k_{ma} is the apparent permeability of matrix α_{m-NF}transfer coefficient between from matrix to natural fracture p_m is the matrix pressure, p_{NF} is the natural fracture pressure and $\mu_g$is gas viscosity.

Unsteady State Models assumes the transient flow between matrix and fracture, the solution is found by doing numerical method, however the solution is the same with the pseudo state model except for the changing period between the matrix-fracture systems.

2.5.2 Triple-porosity model

Triple porosity model was brought forward by Abdussah and Ershaghi (1986); the model has undergone great improvement over the last three decades. Al-ahmadi and Ershaghi (1986) found that this model caters for reservoir heterogeneity. Reservoir heterogeneity refers to dissimilarities of properties in rock formation (Al-Ahmadi & Ershaghi, 1996). Haghshenas et al., (2013) predicted shale gas recovery showing the significance of different porosity configuration. The model was derived from three different triple porosity systems (inorganic matter, organic matter and natural fractures); the models included the diffusion, adsorption/desorption and gas slippage (Haghshenas et al., 2013).

Previous triple continuum models were solved using analytical method approach. In this research numerical methods will be used to solve the model.

CHAPTER 3 PHYSICS AND FLOW MECHANISM OF SHALE GAS RESERVOIR

3.1 Characterisation of the reservoir

The south Karoo Basin's first petro-physical characterisation was performed for the deep borehole KWV-1 which was drilled in 2015 according to the Karoo Research Initiative's (KARIN) scope of work. The KWV-1 was drilled in Eastern Cape Province of South Africa on co-ordinate (32°14'43.10" S, 28°35'08.10" E) (De Kock et al., 2017). The borehole was deep enough to penetrate three super groups; Dwyka, Beafort and Ecca group with their six formations, namely: Koonap Formation (0 m), Waterford Formation (189.2 m), Fort Brown Formation (264.50 m) Fort Rippon Formation (919.20 m), White Formation (2294.95 m) and Prince Formation (2308.40 m) (Campbell et al., 2016).

3.1.1 Methods and materials (Campbell et al., 2016):

The 32 samples were collected, prepared for lithology, pore space and fractures. Petrographic analyses were conducted at Keele University, UK and the Geothermal Laboratory Hydrothermikum was used to do measures of petro and thermophysical rock properties.

Helium pycnometer Accu 1330 and Dry Flo pycnometer Geopyc 1360 were used to measure skeletal density and envelope density respectively to determine porosity.

Conditionally, compressed air was used to measure permeability, the device used, is known as columnar- permeameter from Institute of Applied Geosciences in Germany.

The petro physical rock properties of bore hole KWV-1 are given in Table 3.1. The borehole depth is between 20 m & 30 m for the Ecca Group's White formation show potential for exploration. For development of the model Table 3.1, is used on the parameters mostly of matrix phase and since the parameters determined by (Campbell et al., 2016) are similar to the parameter used by (Guo et al., 2018). Table 3.2 will be used to develop the equations for the natural fracture and hydraulic fracture.

Table 3.1 Petro physical rock properties of the southern Karoo Basin, South Africa (Campbell et al., 2016)

Sample location	KWV-1 (Borehole)	Ecca pass
Number of measurements	32	76
Density range(kg/m3)	2570-2770	2630-2730
Density mean(kg/m3)	2700	2670
Porosity range	0.4-2.2	0-3.7
Porosity mean	1.3	1
Permeability (mD) range	0.001-0.002	0.01-0.1
Permeability (mD) mean	0.05	0.0014

Table 3.2 Basic parameters used for the simulation in Figure 5.2 (Guo et al. 2015, Zhang et al. 2016)

Parameter	Symbol	Value	Units
Reservoir length,		1300	m
Reservoir breadth		600	m
Effective thickness		20	m
Fracture half-length		146	m
Fracture spacing	r_e	200	m
Wellbore radius	r_w	0,1	m
Initial reservoir pressure	p_i	20	MPa
Bottom-hole pressure	p_w	5	MPa
Initial reservoir temperature	T	350	K
Langmuir pressure	p_L	5	MPa
Langmuir volume	V_L	1	m^3/m^3
Porosity of the matrix phase	ϕ_m	0,05	
Porosity of the Natural phase	ϕ_{NF}	0,01	
Porosity of the hydraulic phase	ϕ_{HF}	1	
Matrix permeability	k_{ma}	0,00005	mD
Natural fracture permeability	k_{NF}	0,05	mD
Hydraulic fracture permeability	k_{HF}	8000	mD
NF interface area per unit volume of rock	α_{NF}	50	m^{-1}
HF interface area per unit volume of rock	α_{HF}	0,5	m^{-1}
NF Characteristic length,	L_{NF}	0,1	m
HF Characteristic length,	L_{HF}	1	m
Skin Factor	S	1	
Gas Viscosity,	μ_g	1.265×10^{-5}	Pa.s
Standard molar volume	V_{std}	22,414	m^3/kmol
Molecular Weight	MW	16	kg/kmol

3.2 Shale gas adsorption and desorption

Intricacy of flow in the shale gas reservoir will warrant the incorporation of 2 flow mechanisms in the triple porosity model: adsorption and Klinkenberg effect (the gas slippage flow effect) (Cinco-Ley and Samaniego-V., 1981)

3.2.1 Adsorbed gas

Shale gas has been mentioned early in the literature section that it may be found as free gas in natural fracture and adsorbed gas in the shale and tight rocks' pores. Methane is the main constituent in the composition of the shale gas (±90%), and its molecules are absorbed into the kerogen which is carbon-affinity (Lu et al. 1995, Zhang et al. 2017). Adsorbed gas accounts for sufficiently noteworthy amount of gas in place (GIP) in the reservoir. The adsorbed gas is freed from shale rock surface by drawdown of the formation pressure. This freed gas now becomes free gas which then contributes to the total production of the shale gas. The mass flux of adsorption gas on the surface of pore follows the isotherm adsorption equation (3.1) (Wang et al., 2015):

$$q_{ads} = \frac{\rho_g . MW_g}{V_{std}} . V_{ads} \qquad (3.1)$$

Applying Langmuir adsorption model V_E (equation (3.2)):

$$V_{ads} = \frac{V_L p}{p_L + p} \qquad (3.2)$$

Where: q_{ads} is the mass flux of the adsorbed gas [kg/ (m^3.s)], p [Pa] is the reservoir pressure, p_L and [Pa] is the Langmuir pressure, the pressure proportional to one-half Langmuir volume. V_L[m^3/kg] is Langmuir volume; this is the great gas volume of adsorption at the unlimited pressure. ρ_g[kg/m^3] is the gas density and V_E [m^3 /kg] is adsorbed gas content. V_{std} is the standard conditions mole volume (0°C, 101 325 Pa). MW_g is the molecular mass of the gas. Methane gas has higher composition so the gas molecular mass will be approximated to 16 kg/kmol.

Differentiating q_{ads} from equation (3.2) and applying the Chain Rule Theorem for differentiation of composite functions become

$$\frac{\partial q_{ads}}{\partial t} = \frac{\partial q_{ads}}{\partial p_m} . \frac{\partial p_m}{\partial t} \tag{3.3}$$

$$\frac{\partial q_{ads}}{\partial t} = \frac{\partial}{\partial p_m}\left(\frac{\rho_g M_g}{V_{std}} . \frac{V_L p_m}{p_L + p_m}\right) . \frac{\partial p_m}{\partial t} \tag{3.4}$$

Applying Derivative Product Rule:

$$\frac{\partial q_{ads}}{\partial t} = \left(\frac{V_L p_m}{p_L + p_m} . \frac{\partial}{\partial p_m}\left[\frac{\rho_g M_g}{V_{std}}\right] + \frac{p_g M_g}{V_{std}} . \frac{\partial}{\partial p_m}\left[\frac{V_L p_m}{p_L + p_m}\right]\right) . \frac{\partial p_m}{\partial t} \tag{3.5}$$

$$\frac{\partial q_{ads}}{\partial t} = \left(0 + \frac{\rho_g M_g}{V_{std}} . \frac{\partial}{\partial p_m}\left[\frac{V_L p_m}{p_L + p_m}\right]\right) . \frac{\partial p_m}{\partial t} \tag{3.6}$$

$$\frac{\partial q_{ads}}{\partial t} = \left(\frac{\rho_g M_g}{V_{std}} . \frac{\partial}{\partial p_m}\left[\frac{V_L p_m}{p_L + p_m}\right]\right) . \frac{\partial p_m}{\partial t} \tag{3.7}$$

Applying Derivative quotient rule:

$$\frac{\partial q_{ads}}{\partial t} = \left(\frac{\rho_g M_g}{V_{std}} . \left[\frac{\{p_L + p_m\}V_L - \{V_L p_m\}}{\{p_L + p_m\}^2}\right]\right) . \frac{\partial p_m}{\partial t} \tag{3.8}$$

$$\frac{\partial q_{ads}}{\partial t} = \left(\frac{\rho_g M_g}{V_{std}} . \left[\frac{V_L p_L}{\{p_L + p_m\}^2}\right]\right) . \frac{\partial p_m}{\partial t} \tag{3.9}$$

3.3 The gas slippage flow effect

Klinkenberg slippage effect is taken into consideration in this work, because of extremely low permeability and very small pores of the shale gas reservoir. The main use of Klinkenberg is to alter apparent permeability of the gas as function of pressure in the flow equation (Wu et al. 2009, Hao et al. 2017)

$$k_a = k_i\left(1 + \frac{b}{p}\right) \tag{3.10}$$

Where: k_a is the defined as apparent permeability, k_i is the steady permeability, and b is the Klinkenberg factor; it may change as a result of nature of gas and surface pore sizes (Yao et al., 2013). In this work b is steady and it is defined (3.11):

$$b = \frac{4k_i}{2.81708k_i\sqrt{\frac{k_i}{\phi}}}\sqrt{\frac{\pi RT}{2MW_g}} \tag{3.11}$$

Where: ϕ is the porosity of the rock, R is universal gas constant (8 341 Pa m^3/kmol.K), T (K) is temperature of the reservoir,

Where: MW_g is molecular weight of gas in $(\frac{kg}{kmol})$, $R = 8314\ Pa\frac{m^3}{kmol.K}$ is universal gas constant and T is the reservoir temperature in K.

3.3 Viscosity

Calculation procedure for viscosity in this research is based on correlation of temperature of the reservoir and the reference temperatures of the methane since it is the highest constituent of the shale gas.

Calculating viscosity using equation (3.12):

$$\mu_g = \mu_0 \left(\frac{\theta}{\beta}\right)\left(\frac{T}{T_0}\right)^{\frac{3}{2}} \tag{3.12}$$

Where:

$$\theta = 0.555T + \omega$$

$$\beta = 0.555T_0 + \omega$$

$$\mu_g = 0.01265 \text{ cP}$$

Where: μ_g is the viscosity of gas in cP at temperature T of the reservoir. μ_0 is the reference viscosity at reference temperature T_0. ω is the Sutherland constant (Weast, 1984).

3.4 Compressibility factor

Redlich-Kwong-Soave (RKS) correlation is the most accurate state equation and for convenience the procedure to compute follows.

Calculating compressibility factor using equation (3.13):

$$P = \frac{RT}{V-b} - \frac{a\alpha}{V(V-b)} \tag{3.13}$$

Where:

$$a = 0.42748\frac{R^2T_c^2}{P_c}, \qquad b = 0.08664\frac{RT_c}{P_c}, \qquad \alpha = [1 + (0.48157\omega - 0.176\omega^2)(1 - T_r^{0.5})]^2$$

According RKS80 equation 3.13 is used to find A (equation 3.15), and B (equation 3.16) which represents the thermodynamic properties. Define as equation (3.14), (3.15) and (3.16)

$$Z = \frac{PV}{RT} \tag{3.14}$$

$$A = \frac{Pa}{(RT)^2} = 0.42748\alpha \frac{P_r}{T_r^2}, \tag{3.15}$$

$$A = \frac{Pa}{(RT)^2} = 0.42748\alpha \frac{P_r}{T_r^2},$$

$$B = \frac{Pb}{RT} = 0.08664 \frac{P_r}{T_r}, \tag{3.16}$$

then equation 3.13 is changed to equation with compressibility factor (Z) by substituting equation (3.14), (3.15) and (3.16) to form equation (3.17)

$$Z^3 - Z^2 + Z(A - B - B^2) - AB = f(Z) \tag{3.17}$$

(Da-yu et al., 2015)

Equation 3.18 is polynomial, so the equation is solved with iterative method of (Newton-Raphson iteration method).

$$Z_{k+1} = Z_k - \frac{f(Z)}{f'(Z)}$$

Where Z_k, Z_{k+1} are initial and iterated values of compressibility factors.

$$\therefore Z = 0.849$$

CHAPTER 4 MATHEMATICAL MODEL DEVELOPMENT

4.1 Model Assumption (Gholami and Talaie 2010, Guo et al. 2015)

1. Model is constructed as triple-continuum model, namely: Matrix, Natural Fracture and Hydraulic Fracture and Continuity equation will be the basis and the momentum law in the form of Darcy's law for flow in the porous medium.
2. The flow is assumed to be consecutive meaning from one medium to the other, hence from matrix —> natural fracture —> hydraulic fracture.
3. Assume porosity of the shale rock to be steady.
4. The shale rock is incompressible.
5. Klinkenberg factor is accounted for in matrix and natural fracture flows.
6. Adsorbed gas is considered only at matrix.
7. Hydraulic fracturing is one dimensional and the two-media matrix and natural fracture are two dimensional.
8. Assume constant viscosity of the shale gas.
9. Assume no gravity effects.

Using the law of mass conservation of flow for fluids in porous medium, the shale gas flow will be modelled with reference to Figure 4.1.

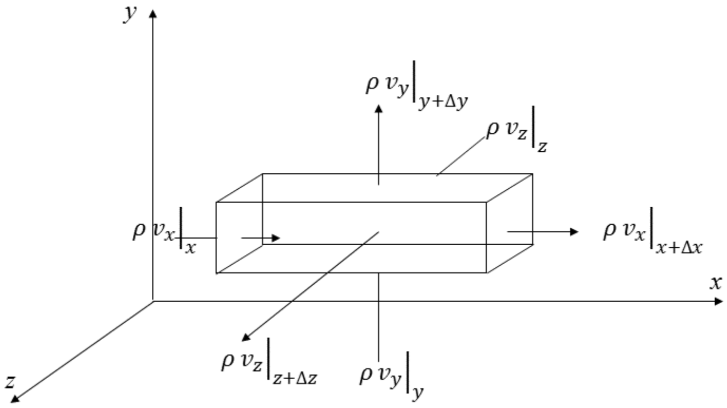

Figure 4.1 Mass flux through a differential control volume

Law of conservation of mass into control volume:

$$\begin{pmatrix} Mass\ flow\ out\ of \\ control\ volume \end{pmatrix} - \begin{pmatrix} Mass\ flow\ into \\ control\ volume \end{pmatrix} + \begin{pmatrix} Rate\ of\ accumulation \\ into\ control\ volume \end{pmatrix} = source\ term$$

(Welty et al., 2008)

In symbols:

$$\iint \rho(\mathbf{v}.\mathbf{n}) + \frac{\partial}{\partial t}\iiint \rho dV = source\ term \tag{4.1}$$

$\iint \rho(\mathbf{v}.\mathbf{n})$ is the rate of mass per unit area passing into and out of the control volume as illustrated by Figure 4.1 therefore, the net mass flux out of the control volume is:

$$(\rho v_x|_{x+\Delta x} - \rho v_x|_x)\Delta y\Delta z + \left(\rho v_y\big|_{y+\Delta y} - \rho v_y\big|_y\right)\Delta x\Delta z + (\rho v_z|_{z+\Delta z} - \rho v_z|_z)\Delta x\Delta y$$

Mass in the control volume is given as$\phi\rho\Delta x\Delta y\Delta z$, the cross-sectional area is constant throughout and hence change is:

$$\frac{\partial}{\partial t}\iiint \rho dV = \frac{\partial}{\partial t}(\phi\rho\Delta x\Delta y\Delta z) \tag{4.2}$$

Summing the net mass rate flux out of control volume and change of mass within control volume. Volume is controlled, meaning there is no change of volume with respect to time. Dividing by $\phi\Delta x\Delta y\Delta z$, and taking the limit as Δx,Δy,Δz,$\rightarrow 0$.

$$\frac{\partial}{\partial x}(\rho v_x) + \frac{\partial}{\partial y}(\rho v_y) + \frac{\partial}{\partial z}(\rho v_z) + \frac{\partial(\phi\rho)}{\partial t} = source\ term \tag{4.3}$$

$$\nabla.\rho\mathbf{v} + \frac{\partial(\phi\rho)}{\partial t} = source\ term \tag{4.4}$$

Equation (4.4) is the general equation for the continuity; this equation will be fundamental basis for deriving the flow equation at matrix continuum, natural fracture and hydraulic fracture.

4.2 The continuity equation in matrix phase

The physical model of the reservoir is drawn below, and the mathematical flow systems of the gas will be derived based on the schematics below, Figure 4.2 and 4.3.

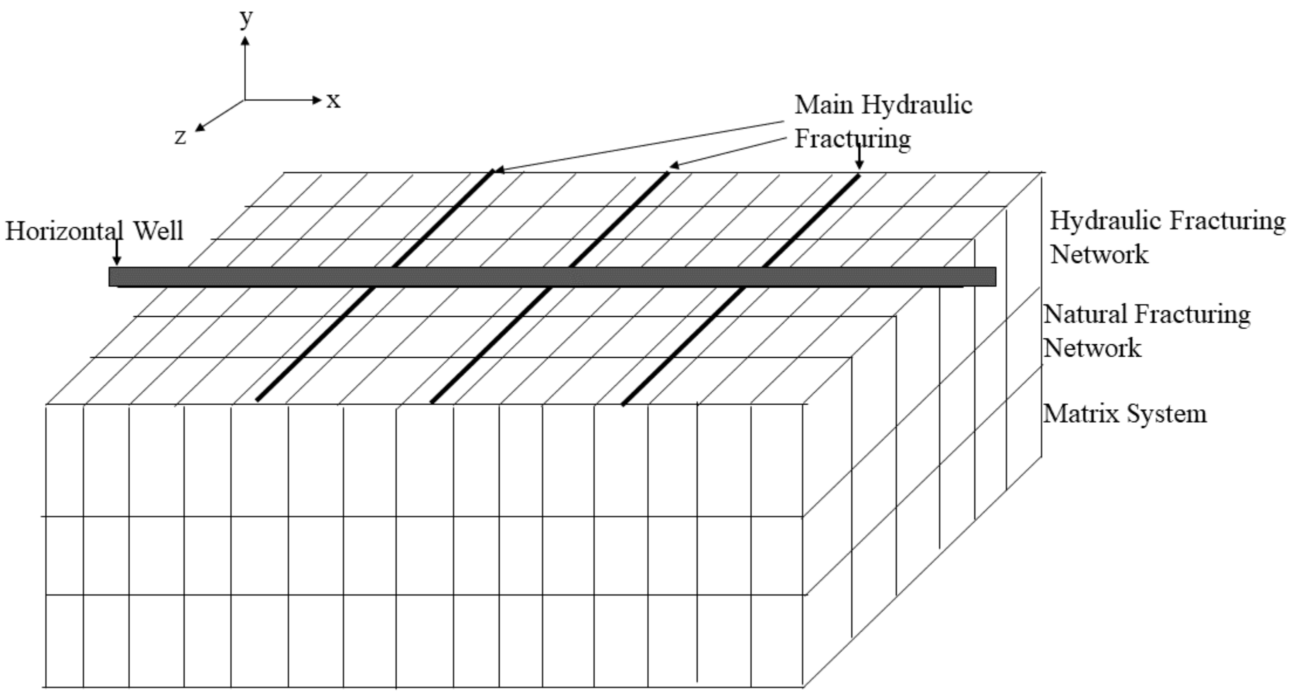

Figure 4.2 Proposed physical triple porosity model (Zhang et al., 2017)

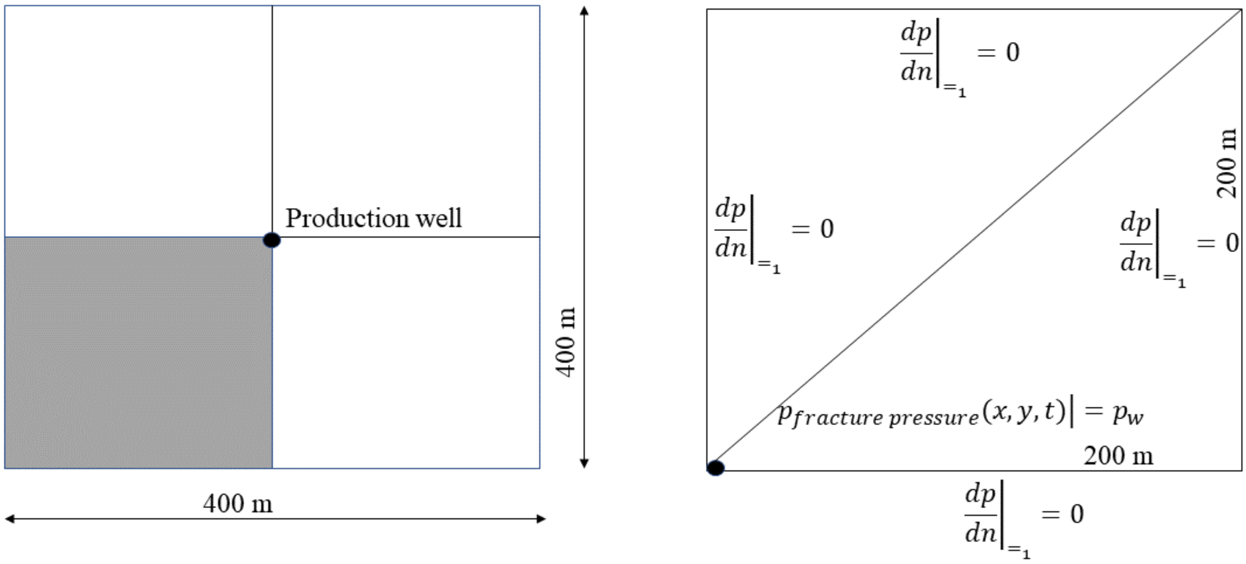

Figure 4.3 Two dimension simplified well simulation model (Guo et al., 2015)

From Equation (4.4),

$$\nabla . \rho \mathbf{v} + \frac{\partial(\phi\rho)}{\partial t} = source\ term \tag{4.5}$$

In the matrix system, gas exists in 2 forms which are the free gas and adsorbed gas:

$$Mass\ of\ gas\ in\ matrix = free\ gas + adsoberd\ gas = \rho_g \phi_m + \rho_g V_E \tag{4.6}$$

Hence the mass accumulation term is as follows:

$$\frac{\partial}{\partial t}\left(\rho_g \phi_m + \rho_g V_E\right) = \frac{\partial}{\partial t}\left(\frac{pM}{zRT}\phi_m\right) + \frac{\partial}{\partial t}\left(\rho_g V_E\right) \tag{4.7}$$

Substituting equation (3.9)

$$\frac{\partial}{\partial t}\left(\rho_g \phi_m + \rho_g V_E\right) = \left(\frac{pM}{zRT}\phi_m + \frac{(1-\phi_m)\rho_g M_g}{V_{std}} . \left[\frac{V_L p_L}{\{p_L + p_m\}^2}\right]\right) . \frac{\partial p_m}{\partial t} \tag{4.8}$$

Assuming 2-Dimensional as stated in the assumption 7

$$\nabla.\rho\mathbf{v} = \left[\frac{\partial}{\partial x}\left(\rho_g v_x\right) + \frac{\partial}{\partial y}\left(\rho_g v_y\right)\right] \tag{4.9}$$

Velocity flow vector term in the matrix:

$$\mathbf{v} = -\frac{1}{\mu_g}\boldsymbol{K}.\left(\nabla p + \rho_g g.\nabla z\right) \tag{4.10}$$

Assuming no effects of gravity due to low density fluid (assumption 9):

$$v_m = -\frac{k_{ma}}{\mu_g}.(\nabla p) \tag{4.11}$$

Simplified for x and y direction

$$v_m = -\frac{k_{ma}}{\mu_g}\left(\frac{\partial p_m}{\partial \mathrm{x}}\right) \tag{4.12}$$

$$v_m = -\frac{k_{ma}}{\mu_g}\left(\frac{\partial p_m}{\partial y}\right) \tag{4.13}$$

$$\frac{\partial}{\partial t}\left(\rho_g \phi_m + \rho_g V_E\right) = -\left[\frac{\partial}{\partial x}\left(\rho_g v_x\right) + \frac{\partial}{\partial y}\left(\rho_g v_y\right)\right] - q_m \tag{4.14}$$

$q_m\left(\frac{kg}{m^3 s}\right)$ is the inter-porosity flow term gas from matrix to natural fracture which takes place in the form of diffusion (Shusheng et al., 2017). The term is expressed as follows by Darcy's law of flow in a porous medium:

$$q_m = \frac{\rho_g k_{ma} \alpha_{m\rightarrow NF}(p_m - p_{NF})}{\mu_g} \tag{4.15}$$

$$\alpha_{m\rightarrow NF} = \frac{A_{m\rightarrow NF}}{L_{NF}} \tag{4.16}$$

Where α_{mf} is the shape factor, from a matrix (m) to natural fracture (NF), $A_{m\rightarrow NF}$ is the interface area from matrix to NF and L_f is the characteristic length of NF. The spacing is generally in the range of 0.05 to 10 metres (Bustin et al., 2008)

The flow term in the matrix media is derived from the general Darcy's equation derived from Naiver-Stokes Equation is given below:

$$k_{ma} = k_{mi}\left[1 + \frac{b_m}{p_m}\right] \tag{4.17}$$

$$\rho_g = \frac{MW.p}{RTZ} = \beta p = 6.4156 \times 10^{-3} p \tag{4.18}$$

Substituting equation 4.8-4.13 into the matrix system continuity equation (4.14):

$$\left(\frac{p_m M_g}{zRT}\phi_m + \frac{(1-\phi_m)\rho_g M_g}{V_{std}}.\left[\frac{V_L p_L}{\{p_L + p_m\}^2}\right]\right).\frac{\partial p_m}{\partial t} = -\left(\frac{\partial}{\partial x}\left[\frac{p_m M_g}{zRT}. -\frac{k_{ma}}{\mu_g}\frac{\partial p_m}{\partial x}\right] + \frac{\partial}{\partial y}\left[\frac{p_m M_g}{zRT}. -\frac{k_{ma}}{\mu_g}\frac{\partial p_m}{\partial y}\right]\right) - \frac{\rho_g k_{ma}\alpha_{m\rightarrow NF}(p_m - p_{NF})}{\mu_g} \tag{4.19}$$

Simplifying taking ρ_g as constant:

$$\left(\phi_m + \frac{(1-\phi_m)M_g}{V_{std}}.\left[\frac{V_L p_L}{\{p_L + p_m\}^2}\right]\right).\frac{\partial p_m}{\partial t} = \frac{k_{ma}}{\mu_g}\frac{\partial^2 p_m}{\partial x^2} + \frac{k_{ma}}{\mu_g}\frac{\partial^2 p_m}{\partial y^2} - \frac{k_{ma}\alpha_{m\rightarrow NF}(p_m - p_{NF})}{\mu_g} \tag{4.20}$$

Referring to Appendix A, parameters in equation (4.20) were substituted from data collected by (Guo et al., 2015) to determine equation (4.11). Table 3.2 is also used to substitute some of the parameters.

$$0.05\frac{\partial p_m}{\partial t} = 3.90087\times10^{-15}\frac{\partial^2 p_m}{\partial x^2} + 3.90087\times10^{-15}\frac{\partial^2 p_m}{\partial x^2} - 1.95043\times10^{-16}(20\times10^6 - p_{NF}) \tag{4.21}$$

Initial boundary: $p_m = p_i = 20\ MPa; t = 0$

Boundary condition: $\frac{\partial p_m}{\partial n}_{\Gamma} = 0; t > 0$

4.3 The continuity equation of natural fracture phase

General equation form:

$$\nabla.\rho\mathbf{v} + \frac{\partial(\phi\rho)}{\partial t} = source\ term \tag{4.22}$$

Due to free gas only in the natural fracture system, hence for accumulation term:

$$\frac{\partial}{\partial t}(\rho_g\phi_{NF}) \tag{4.23}$$

Flow vector term:

$$\frac{\partial}{\partial x}(\rho_g v_x) - \frac{\partial}{\partial y}(\rho_g v_y) \tag{4.24}$$

For interporosity term from matrix system to natural fracture system:

$$q_m - q_{NF} \tag{4.25}$$

Continuity equation of the natural fracture

$$q_m - q_{NF} \tag{4.26}$$

$$\frac{\partial}{\partial t}(\rho_g\phi_{NF}) = q_m - q_{NF} - \frac{\partial}{\partial x}(\rho_g v_x) - \frac{\partial}{\partial y}(\rho_g v_y) \tag{4.27}$$

Where q_{NF} is the inter-porosity flow term of gas from the natural fracture to the hydraulic fracture

$$q_{\boldsymbol{NF}} = \frac{\rho_g k_{NFa} \alpha_{NF\to HF}(p_{NF} - p_{HF})}{\mu_g} \tag{4.28}$$

Where $\alpha_{NF}$is the shape factor from natural fracture to hydraulic, interface area of natural fracture and hydraulic per unit volume divide by characteristics length of hydraulic. $\alpha_{NF\to HF} = \frac{A_{NF\to HF}}{L_{HF}}$.

Applying differentiation product rule, therefore natural fracture flow general equation:

$$\frac{\partial}{\partial t}(\rho_g \phi_{NF}) = \frac{\rho_g k_{ma} \alpha_{m\to NF}(p_m - p_{NF})}{\mu_g} \frac{\rho_g k_{NFa} \alpha_{NF\to HF}(p_{NF} - p_{HF})}{\mu_g} + \frac{\partial}{\partial x}\left[\beta p_{NF} \frac{k_{NF}}{\mu_g} \frac{\partial p_{NF}}{\partial x}\right] + \frac{\partial}{\partial y}\left[\beta p_{NF} \frac{k_{NF}}{\mu_g} \frac{\partial p_{NF}}{\partial y}\right] \tag{4.29}$$

Klinkenberg factor in natural fracture

$$k_{NFa} = k_{NFi}\left[1 + \frac{b_{NF}}{p_{NF}}\right] \tag{4.30}$$

$$b_{NF} = \frac{4k_{NFi}}{2.81708 k_{NFi}\sqrt{\frac{k_{NFi}}{\Phi_{NF}}}}\sqrt{\frac{\pi RT}{2M_g}} \tag{4.31}$$

Substituting equation (4.29) and (4.30) into equation (4.28):

$$\beta \phi_{NF} \frac{\partial p_{NF}}{\partial t} = \frac{\beta k_{ma} \alpha_{m\to NF} p_{NF}(p_m - p_{NF})}{\mu_g} - \frac{\beta k_{NFa} \alpha_{NF\to HF} p_{HF}(p_{NF} - p_{HF})}{\mu_g} + \frac{\partial}{\partial x}\left[\beta p_{NF} \frac{k_{NF}}{\mu_g} \frac{\partial p_{NF}}{\partial x}\right] + \frac{\partial}{\partial y}\left[\beta p_{NF} \frac{k_{NF}}{\mu_g} \frac{\partial p_{NF}}{\partial y}\right] \tag{4.32}$$

$$\phi_{NF} \frac{\partial p_{NF}}{\partial t} = \frac{k_{ma} \alpha_{m\to NF} p_{NF}(p_m - p_{NF})}{\mu_g} - \frac{k_{NFa} \alpha_{NF\to HF} p_{HF}(p_{NF} - p_{HF})}{\mu_g} + \frac{\partial}{\partial x}\left[p_{NF} \frac{k_{NF}}{\mu_g} \frac{\partial p_{NF}}{\partial x}\right] + \frac{\partial}{\partial y}\left[p_{NF} \frac{k_{NF}}{\mu_g} \frac{\partial p_{NF}}{\partial y}\right] \tag{4.33}$$

$$0.01\frac{\partial p_{NF}}{\partial t} = 2.00\times10^{-15}(20\times10^{6} - p_{NF}) - 2.00\times10^{-9}(20\times10^{6} - p_{HF}) + \frac{\partial}{\partial x}\left[7.80\times10^{-5}\frac{\partial p_{NF}}{\partial x}\right] + \frac{\partial}{\partial y}\left[7.80\times10^{-5}\frac{\partial p_{NF}}{\partial y}\right] \quad (4.34)$$

Initial boundary:

$$p_{NF} = p_i = 20\ MPa; t = 0$$

Boundary condition:

$$\frac{\partial p_{NF}}{\partial n}_{\Gamma} = 0; t > 0$$

4.4 The flow equation for the hydraulic fracture phase

Hydraulic fracturing is quite different from matrix and natural fracture because they are discretely distributed on the field of the reservoir (Zhang, et al., 2016). The flow of the hydraulic fracture is considered as 1 dimensional flow. The desorption and Klinkenberg effect do not form part of the flow equation. Natural fracture, thus the continuity equation reduces to;

$$\frac{\partial p_{HF}}{\partial t}(\rho_g \phi_{HF}) = q_{NF} - q_{HF\to w} - \frac{\partial}{\partial y}(\rho_g v_y) \quad (4.35)$$

Where $q_{HF-w}\left[\frac{kg}{m^3 s}\right]$ is the flow parameter from hydraulic fracture to the horizontal well. It is applied where the grids of HF intersect with horizontal well, assuming steady production (Zhang et al., 2016). The flow in hydraulic fracture is modelled as radial flow, which is depicted by Figure 4.4

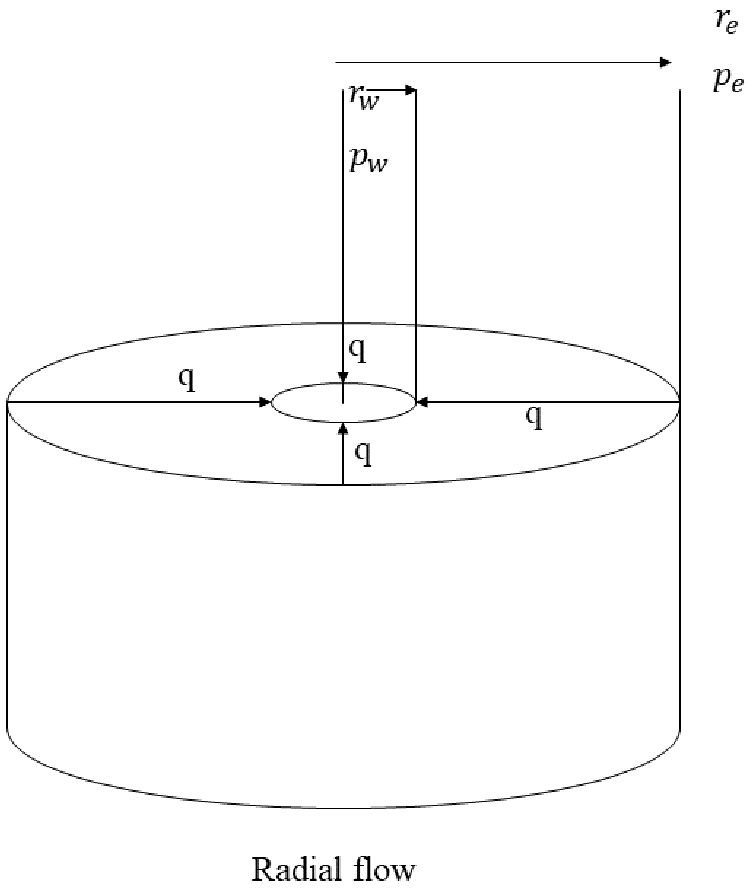

Figure 4.4 the radial flow schematic diagram

$$q_{HF-w} = \frac{q}{V_{i,j}} = \frac{2\pi\rho_g k_{HF-a}\left(p_{HF\ i,j} - p_{HF-w}\right)}{\Delta x \Delta y \mu_g \ln\frac{r_e}{r_{NF-w}}}\ (grid\ intersect\ with\ well\ bore) \tag{4.36}$$

$$q_{HF-w} = 0(other\ HF\ grids) \tag{4.37}$$

Where $q\left[\frac{kg}{s}\right]$ is the gas production rate, $V_{i,j}$volume of the grid of which the HF intersect with the well bore.

$$q = \frac{2\pi h k_{HF}\left(p_{HF\ i,j} - p_{HF-w}\right)}{\mu_g \ln\frac{r_e}{r_{NF-w}} + S - 0.75}, \qquad r_e = 0.14\sqrt{\Delta x^2 + \Delta y^2} \tag{4.38}$$

(Dake, 1978)

q_{HF} is the interporosity flow parameter from natural fracture to hydraulic fracture, applied at the grids HF since HF receives feed from the natural fracture system (Zhang et al., 2016). Substituting equation (4.4), (4.12) and (4.20) into equation (4.19) yield:

$$-\frac{\partial}{\partial y}\left[\frac{p_{HF}MW}{ZRT}.\left(-\frac{k_{HF-a}}{\mu_g}\frac{\partial p_{HF}}{\partial y}\right)\right]+\frac{\rho_g k_{NFa}\alpha_{NF}(p_{NF}-p_{HF})}{\mu_g}-\frac{2\pi\rho_g k_{HF-a}\left(p_{HF\,i,j}-p_{HF-w}\right)}{\Delta x\Delta y\mu_g \ln\frac{r_e}{r_{NF-w}}}=\left[\frac{\phi_{HF}MW}{ZRT}\right]\frac{\partial p_{HF}}{\partial t} \quad (4.39)$$

$$-\frac{\partial}{\partial y}\left[\frac{p_{HF}MW}{ZRT}.\left(-\frac{k_{HF}}{\mu_g}\frac{\partial p_{HF}}{\partial y}\right)\right]+\frac{p_{HF}MW.k_{NFa}\alpha_{NF\rightarrow HF}(p_{NF}-p_{HF})}{ZRT\mu_g}-\frac{2\pi p_{HF}MW.k_{HF\rightarrow a}(p_{HF}-p_{HF-w})}{ZRT.\Delta x\Delta y\mu_g \ln\frac{r_e}{r_{NF-w}}}$$
$$=\left[\frac{\phi_{HF}MW}{ZRT}\right]\frac{\partial p_{HF}}{\partial t} \quad (4.40)$$

Simplifying:

$$-\frac{\partial}{\partial y}\left[p_{HF}\cdot\left(-\frac{k_{HF-a}}{\mu_g}\frac{\partial p_{HF}}{\partial y}\right)\right]+\frac{p_{HF}.k_{NFa}\alpha_{NF}(p_{NF}-p_{HF})}{\mu_g}-\frac{2\pi p_{HF}.k_{HF-a}\left(p_{HF\,i,j}-p_{HF-w}\right)}{\Delta x\Delta y\mu_g \ln\frac{r_e}{r_{NF-w}}}=[\phi_{HF}]\frac{\partial p_{HF}}{\partial t} \quad (4.41)$$

$$\frac{\partial}{\partial y}\left[\frac{k_{HF-a}p_{HF}}{\mu_g}\frac{\partial p_{HF}}{\partial y}\right]+\frac{p_{HF}.k_{NFa}\alpha_{NF\rightarrow HF}(p_{NF}-p_{HF})}{\mu_g}-\frac{2\pi p_{HF}.k_{HF-a}(p_{HF}-p_{HF\rightarrow w})}{\Delta x\Delta y\mu_g\, ln\frac{r_e}{r_{NF-w}}}=[\phi_{HF}]\frac{\partial p_{HF}}{\partial t} \quad (4.42)$$

Appendix C shows how basic parameters from the literature were substituted and calculations were carried out on the excel spreadsheet to determine equation (4.27)

$$\frac{\partial}{\partial y}\left[0.1248269\frac{\partial p_{HF}}{\partial y}\right]+0.1248269(20\times 10^6-p_{HF})-4.98\times 10^{-4}=\frac{\partial p_{HF}}{\partial t} \quad (4.43)$$

Initial boundary:

$$p_{HF}(0<x<1\,300m, t=0)=20\times 10^6\ Pa$$

Outer boundary condition:

$$p_{HF}(x=0\ m, t>0)=p_i=20\times 10^6\ Pa$$

$$\left.\frac{\partial p_m}{\partial n}\right|_{\Gamma} = 0; t > 0$$

Inner boundary condition:

$$p_{HF}(x = 1\ 300\ m, t > 0) = 5 \times 10^6\ Pa$$

$$q_{HF-w} = \frac{q}{V_{i,j}} = \frac{2\pi\rho_g k_{HF}(p_{HF} - p_{HF-w})}{\Delta x \Delta y \mu_g \left[\ln\left(\frac{r_e}{r_{NF-w}}\right) + S - \frac{3}{4}\right]};\ t(s) > 0$$

CHAPTER 5 SOLUTION TO THE MODEL USING MATLAB CODING

The derived triple-continuum mathematical model (equation (4.43), (4.33) and (4.21)) is solved by a numerical method known as the finite difference method (FDM). The equations are solved explicitly because of discretisation of the partial differential equations (PDEs). Discretisation is placement of many nodes using grid generation techniques.

The equations (4.43), (4.33) and (4.21) are second order linear PDEs and are generically classified into 3 types: Elliptic, parabolic and hyperbolic. Equation (4.43) is a one-dimensional (1D) diffusion equation meaning that it is a time dependent pressure distribution along a pressurised (hydraulic fracking) 1D area. Equation (4.33) and (4.21) are 2-D diffusion equations meaning that they are also time dependent - pressure distribution.

The model will be solved by firstly the solving hydraulic fracture (4.43) to find p_{HF} (on section 5.1) and secondly substituting it into the natural facture equation to find p_{NF} (on section 5.2). Then thirdly substitute p_{HF} and p_{NF} into the matrix equation (4.21) to obtain p_m (section 5.3). The above solving algorithm is applied on the MATLAB program (see section 5.4).

5.1 Hydraulic fracture phase

$$\frac{\partial}{\partial y}\left[0.1248269\frac{\partial p_{HF}}{\partial y}\right] + 0.1248269(20 \times 10^6 - p_{HF}) - 4.98 \times 10^{-4} = \frac{\partial p_{HF}}{\partial t} \tag{4.43}$$

Initial boundary:

$$p_{HF}(0 < x < 1\,300m, t = 0\ sec) = p_i = 20 \times 10^6\ Pa$$

Outer boundary condition:

$$p_{HF}(x = 0\ m, t > 0\ sec) = p_i = 20 \times 10^6\ Pa$$

$$\frac{\partial p_m}{\partial n}_{\Gamma} = 0; t > 0\ sec$$

Inner boundary condition:

$$p_{HF}(x = 1\,300\ m, t > 0\ sec) = 5 \times 10^6\ Pa$$

Equation (4.43) is of the general diffusion equation in 1 D:

$$\frac{\partial p}{\partial t} = \kappa \frac{\partial^2 p}{\partial y^2} + F(y,t)$$

- p (y, t): the unknown function we want to find
- κ: the known constant
- F (y, t): the known pressure source distribution

Derivatives approximated by finite difference method:

$$\frac{\partial p}{\partial t} \approx \frac{p_i^{l+1} - p_i^l}{\Delta t}$$

$$\frac{\partial^2 p}{\partial y^2} \approx \frac{p_{i-1}^l - 2p_i^l + p_{i+1}^l}{\Delta y^2}$$

Therefore, the approximation of the finite difference method:

$$\frac{p_i^{l+1} - p_i^l}{\Delta t} = \frac{p_{i-1}^l - 2p_i^l + p_{i+1}^l}{\Delta y^2} + F(y_i, t_l) \tag{5.1}$$

Explicit method:

$$p_i^{l+1} = p_i^l + \kappa \frac{\Delta t}{\Delta y^2}\left(p_{i-1}^l - 2p_i^l + p_{i+1}^l\right) + \Delta t F(y_i, t_l);\ 0 < \kappa \frac{\Delta t}{\Delta y^2} < 0.5 \tag{5.2}$$

$$p_i^{l+1} = p_i^l + \kappa \frac{\Delta t}{\Delta y^2}\left(p_{i-1}^l - 2p_i^l + p_{i+1}^l\right) + \Delta t\left[0.1248269\left(20 \times 10^6 - p_i^l\right) - 4.98 \times 10^{-4}\right] \tag{5.3}$$

5.2 Natural fracture phase

$$0.01 \frac{\partial p_{NF}}{\partial t} = 2.00 \times 10^{-15}(20 \times 10^6 - p_{NF}) - 2.00 \times 10^{-9}(20 \times 10^6 - p_{HF}) + \frac{\partial}{\partial x}\left[7.80 \times 10^{-5} \frac{\partial p_{NF}}{\partial x}\right] + \frac{\partial}{\partial y}\left[7.80 \times 10^{-5} \frac{\partial p_{NF}}{\partial y}\right] \tag{4.33}$$

Initial boundary:

$$p_m(0 < x < 1\,300 m, t = 0\ sec) = 20 \times 10^6\ Pa$$

Outer boundary condition:

$$p_m(x = 0\ m, t > 0\ sec) = p_i = 20 \times 10^6\ Pa$$

$$\frac{\partial p_m}{\partial n}_{\Gamma} = 0; t > 0\ sec$$

Inner boundary condition:

$$p_m(x = 1\ 300\ m, t > 0\ sec) = 5 \times 10^6\ Pa$$

Equation (4.11) is of the general heat equation in 2 D:

$$\frac{\partial p}{\partial t} = \kappa \left(\frac{\partial^2 p}{\partial x^2} + \frac{\partial^2 p}{\partial y^2} \right) + F(y, t) \tag{5.4}$$

- p (y, t): the unknown function we want to find
- κ: the known constant
- F (y, t): the known source distribution

Derivatives approximated by finite difference method:

$$\frac{\partial p}{\partial t} \approx \frac{p_i^{m+1} - p_i^m}{\Delta t} \tag{5.5}$$

$$\frac{\partial^2 p}{\partial y^2} \approx \frac{p_{i-1}^l - 2p_i^l - p_{i+1}^l}{\Delta y^2} \tag{5.6}$$

Therefore, the approximation of the finite difference method:

$$\frac{p_{i,j}^{m+1} - p_{i,j}^l}{\Delta t} = \kappa \left(\frac{p_{i,j-1}^m - 2p_i^m + p_{i,j+1}^m}{\Delta x^2} + \frac{p_{j,i-1}^m - 2p_{i,j}^m + p_{i,j+1}^m}{\Delta y^2} \right) + F(y_{i,j}, x_{i,j} t_m) \tag{5.7}$$

Explicit method solution:

$$p_{i,j}^{m+1} = p_{i,j}^m + \kappa \frac{\Delta t}{\Delta x^2} \left(p_{i,j-1}^m - 2p_{i,j}^m + p_{i,j+1}^m \right) + \kappa \frac{\Delta t}{\Delta y^2} \left(p_{j,i-1}^m - 2p_{i,j}^m + p_{i,j+1}^m \right) + \Delta t F(y_{i,j}, x_{i,j} t_m) \tag{5.8}$$

$$p_{i,j}^{m+1} = p_{i,j}^m + \kappa \frac{\Delta t}{\Delta x^2} \left(p_{i,j-1}^m - 2p_i^m + p_{i,j+1}^m \right) + \kappa \frac{\Delta t}{\Delta y^2} \left(p_{j,i-1}^m - 2p_{i,j}^m + p_{j,i+1}^m \right) + \Delta t \left[2.00 \times 10^{-15} \left(20 \times 10^6 - p_{i,j}^m \right) - 2.00 \times 10^{-9} \left(20 \times 10^6 - p_i^{l+1} \right) \right] \tag{5.9}$$

5.3 Matrix phase

$$0.05 \frac{\partial p_m}{\partial t} = 3.90087 \times 10^{-15} \frac{\partial^2 p_m}{\partial x^2} + 3.90087 \times 10^{-15} \frac{\partial^2 p_m}{\partial x^2} - 1.95043 \times 10^{-16} (20 \times 10^6 - p_{NF}) \tag{4.21}$$

Initial boundary:

$$p_m(0 < x < 1\ 300 m, t = 0\ sec) = 20 \times 10^6\ Pa$$

Outer boundary condition:

$$p_m(x = 0\ m, t > 0\ sec) = p_i = 20 \times 10^6\ Pa$$

$$\frac{\partial p_m}{\partial n}_{\Gamma} = 0; t > 0\ sec$$

Inner boundary condition:

$$p_m(x = 1\ 300\ m, t > 0\ sec) = 5 \times 10^6\ Pa$$

Equation 14.1 is also 2 D; it follows the same derivation of the Equation 20.1 to be the finite difference equation:

$$p_{i,j}^{n+1} = p_{i,j}^{n} + \kappa \frac{\Delta t}{\Delta x^2}\left(p_{i,j-1}^{n} - 2p_{i,j}^{n} + p_{i,j+1}^{n}\right) + \kappa \frac{\Delta t}{\Delta y^2}\left(p_{j,i-1}^{n} - 2p_{i,j}^{n} + p_{i,j+1}^{n}\right) + \Delta t\left[1.95043 \times 10^{-16}(20 \times 10^6 - p_{i,j}^{m})\right] \tag{5.10}$$

5.4 MATLAB code

After solving Equation (4.43), (4.33) and (14.21) using the finite difference method (explicitly), the code was developed to show the reservoir pressure in hydraulic fracture, natural fracture and matrix phase, the MATLAB code is on Appendix D (hydraulic fracture), E (natural fracture) and F (matrix phase). Figure 5.1 simulates hydraulic fracture, 5.2 natural fracture and 5.3 matrix phase.

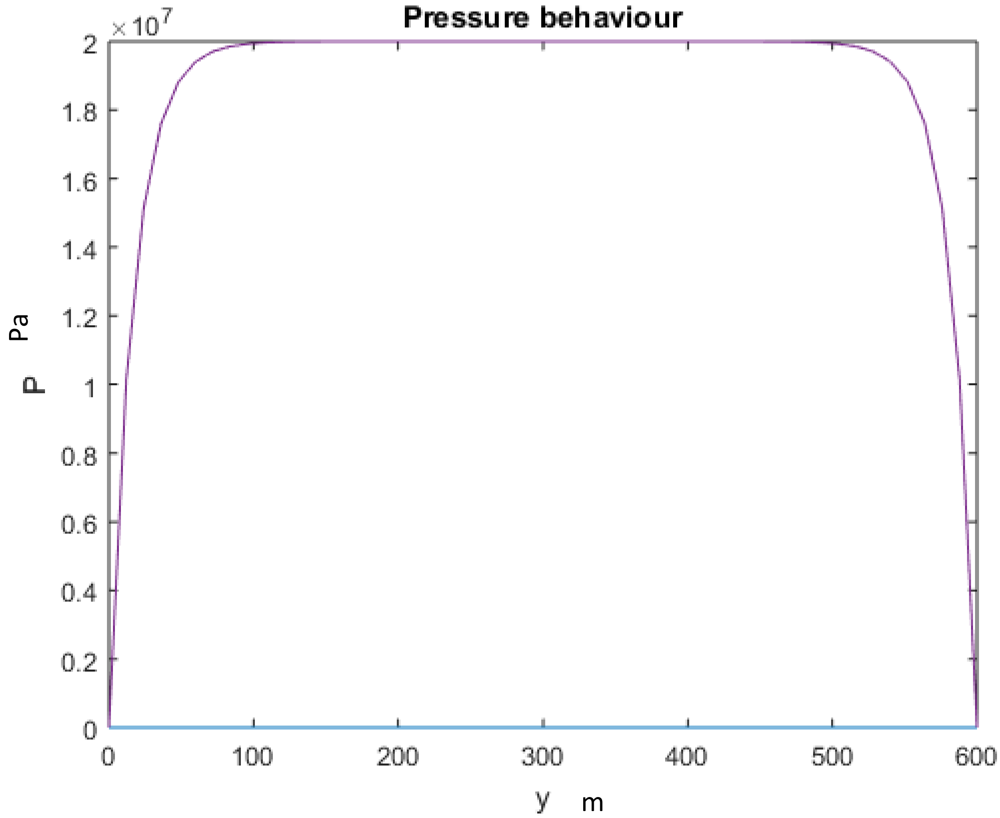

Figure 5.1 Pressure distributions along the reservoir according to the hydraulic fracture

Figure 5.1 illustrates fracture propagation and simulation of the shale gas flow in the reservoir as depicted by Figure 4.2 and Figure 4.3 This propagation of fractures is due to the pressure gradient of hydraulic fracturing, which is prompted by convergence between the hydraulic fractures and the porous rock medium (natural fracturing). This is a strain concentration at fracture tips meaning that the strain increases with increasing pressure gradient (Santillán et al., 2018).

Hydraulic fracturing propagates at the straight-line path on the pressure profile which is between 100m and 500m. At this stage (length between 100 m and 500 m) of hydraulic fracking, propagation is at steady length. This is at this length, where production can take place, after 500m the pressure decreases, and propagation stops.

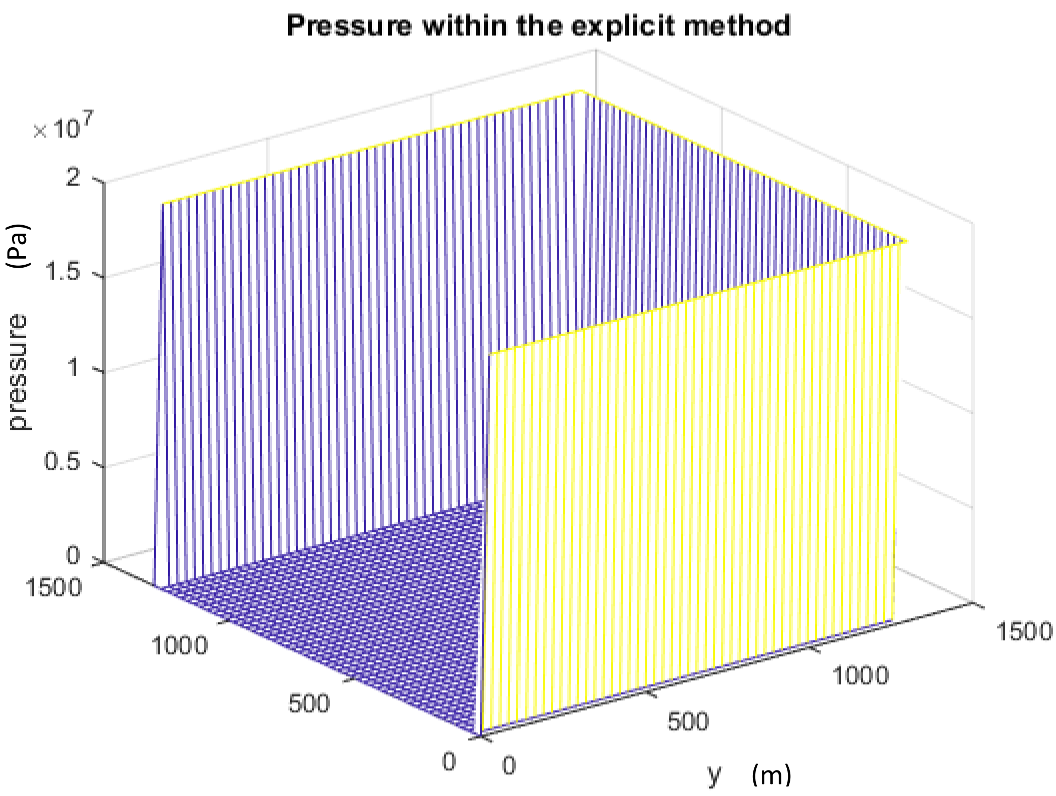

Figure 5.2 Pressure diffusion along the reservoir in the natural fracture

Figure 5.2 illustrates the natural fracture pressure profile. Before hydraulic fracture takes place there is little propagation, the flow of shale gas is insignificant as compared to the hydraulic fracturing. In this phase (natural fracture), propagation is due to the permeability of the rock. Hence at this phase Figure 5.2 displays a cuboidal shape containing trapped gas. When propagation takes place the fluid fracture decreases.

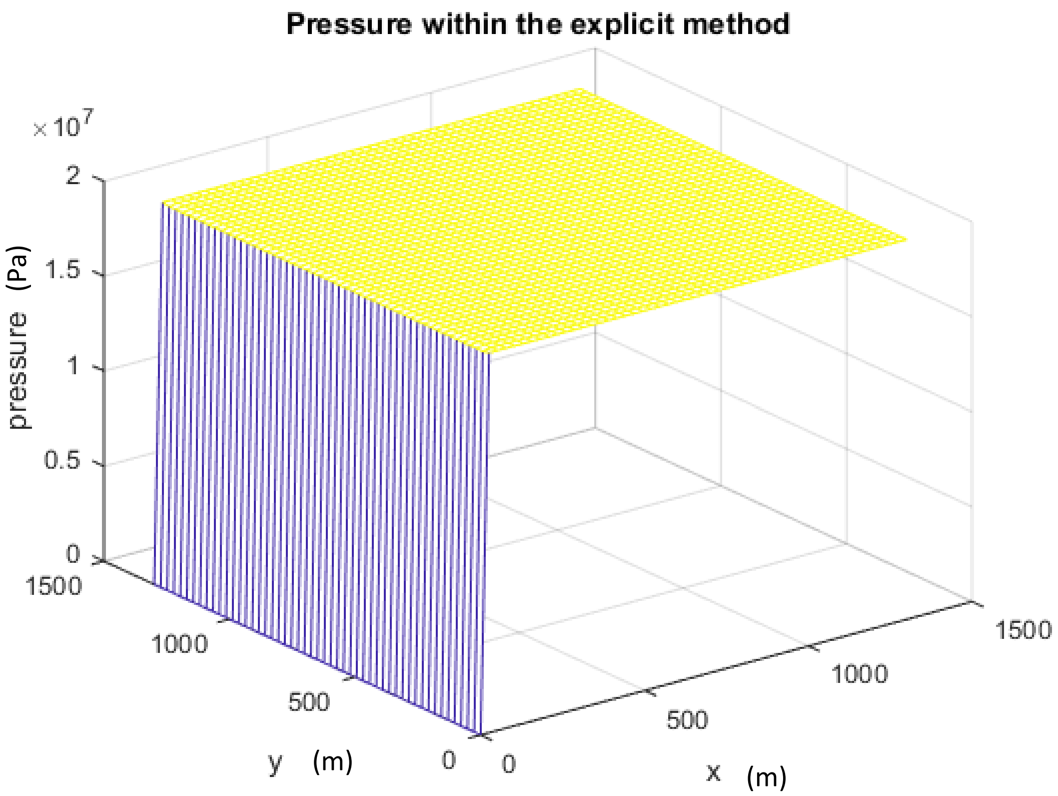

Figure 5.3 Pressure distribution in the matrix phase

Figure 5.3 shows the pressure profile of reservoir. This profile displays pressure of well using grid model (matrix). This model depicts the gas on the rocks. The gas on the rocks is the absorbed gas. During fracking this is the gas that travels from the rock to the opening of the rocks (hydraulic fracture system) which then makes up the original gas in place.

CHAPTER 6 MODEL VERIFICATION

Currently South Africa's Karoo region does not have field data and hence the model is treated as a theoretical case. In general, the method followed to verify the validity of the model is the comparison of the field data from the Barnett shale reservoir. The Barnett shale reservoir field data is compared with the model. This validation is done to ensure that the model developed in this report gives reliable results which will be explored in the sensitivity and results analysis section. The field data used comes from (Grieser et al., 2009) publication. This data was used to develop the multistage hydraulic fracturing of the horizontal well of Barnett, Figure 6.2 (Guo et al., 2018). The multi stage of the horizontal reservoir is shown in Figure 6.1 and the parameters employed in the simulation are given from Table 3.2. The basic reservoir parameters are collected from the literature randomly (Zhang et al., 2016).

Figure 6.1, a physical model of the reservoir, characterises and simulates the gas flow in the matrix phase, natural phase and to the hydraulic fractures. The physical model simulates the reservoir with the length of 1300 m, the width of 400 m and the thickness of 20 m (De Kock et al., 2017). The mesh grid size is 200 mx200 mx1m dimensions in the direction of x, y and z, respectively. Figure 6.2 is the simulation of the developed model in this report, and it is compared to the field and the simulated model by (Guo et al., 2018). The model is comparable with minimal deviation, at the less than 400 days the production rate is still approximately greater than or equivalent to 1.5 Million standard cubic feet of gas per day (MMSCFD). For this validation the Hydraulic fracture phase is employed.

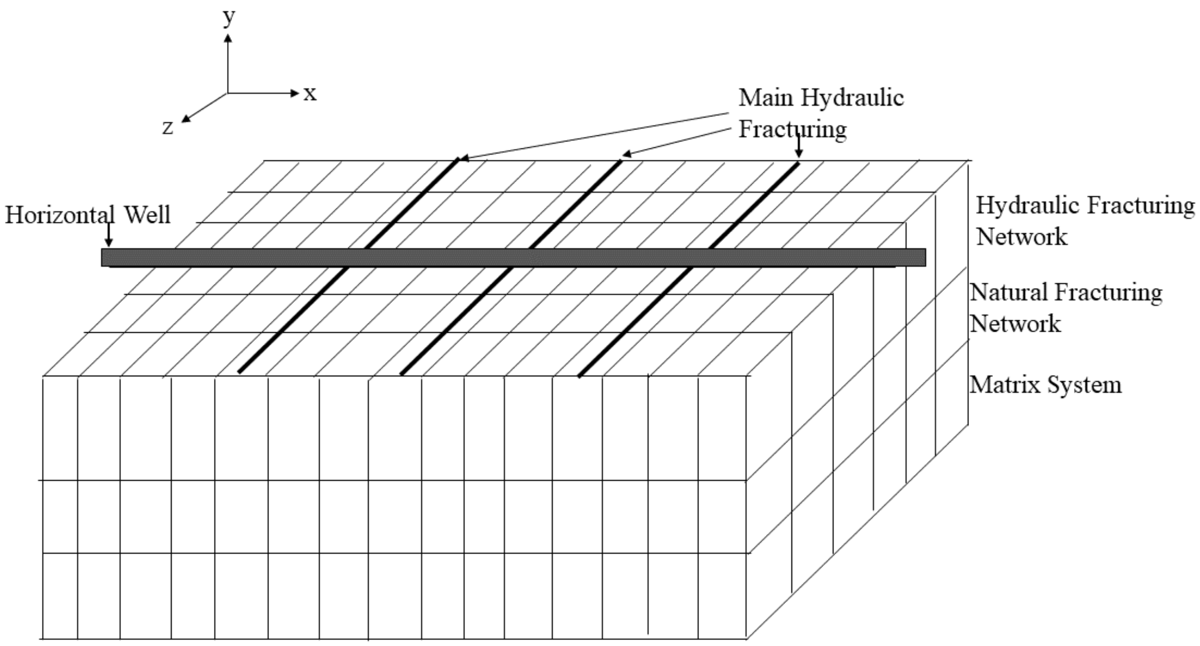

Figure 6.1 Physical model of the reservoir, bore hole KWV-1 (Main South Karoo)

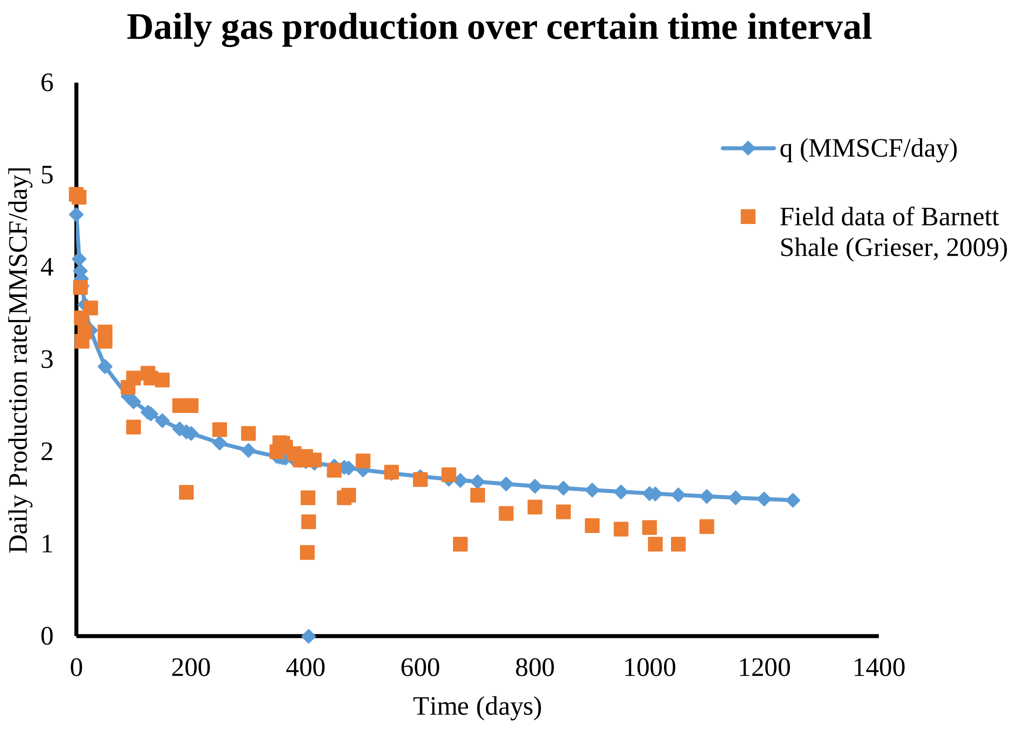

Figure 6.2 Field data of Barnett Shale and simulation data developed

Statistical test for the model

The model was further validated using the t-test method to establish the 95% confidence interval; Table 6.1 shows important variables that statistically validates the method. The calculations were performed using Microsoft Excel Spreadsheet tool called Data Analysis. The calculations are shown in Appendix G.

Table 6.1 t-Test: Two-Sample Assuming Unequal Variances

	Variable 1	*Variable 2*
Mean	1.86533333	1.502708333
Variance	1.0474401	1.304007402
Observations	48	48
Hypothesized Mean Difference	0	
df	93	
t Stat	1.63836521	
P(T<=t) one-tail	0.05236229	
t Critical one-tail	1.66140367	
P(T<=t) two-tail	0.10472458	
t Critical two-tail	1.98580181	

Two-tail test (inequality) was performed. 1) t Stat < -t Critical two-tail or 2) t Stat > t Critical two-tail, therefore the null hypothesis is rejected. This is not the case, -1.985< 1.638< 1.985. Therefore, the null hypothesis is not rejected. The observed difference between the samples means (1.865 - 1.503) does have enough evidence that the average production rate between field data and model data differ significantly.

CHAPTER 7 SENSITIVITY ANALYSIS

In the sensitivity analysis the model used was a combination of the radial flow equation (Equation 4.27) and the Arp's equation for general decline in a well (Equation (7.1)).

$$q(t)(\frac{m^3}{day}) = \frac{q_i}{(1 + bD_i t)^{\frac{1}{b}}} \tag{7.1}$$

Whereby q_i is the initial production rate (volume/day), $q(t)$ is the production rate at time t (day), b is the nominal exponential decline rate, and D_i is the rate of initial decline.

In this study 3 parameters are studied. This includes:

- the permeability of hydraulic fracture (k_{HF})
- the drainage radius (r_e)
- the initial pressure ($p_m = p_{NF} = p_{HF} = p_i$)

For each parameter 3 stages of changes were compared to the production rate and the total cumulative gas production rate.

7.1 The effect of changing the permeability of hydraulic fracture (k_{HF}) against the production rate

Figure 7.1 and Figure 7.2 shows the relationship of various rates of gas production against time and total cumulative gas production rate, respectively. This comparison is made for different hydraulic permeabilities. The comparison is made from 3 permeabilities; at the permeability of k_{HF} = 60 mD, k_{HF}= 80 mD and k_{HF} = 100 mD (Zhang, et al., 2016)

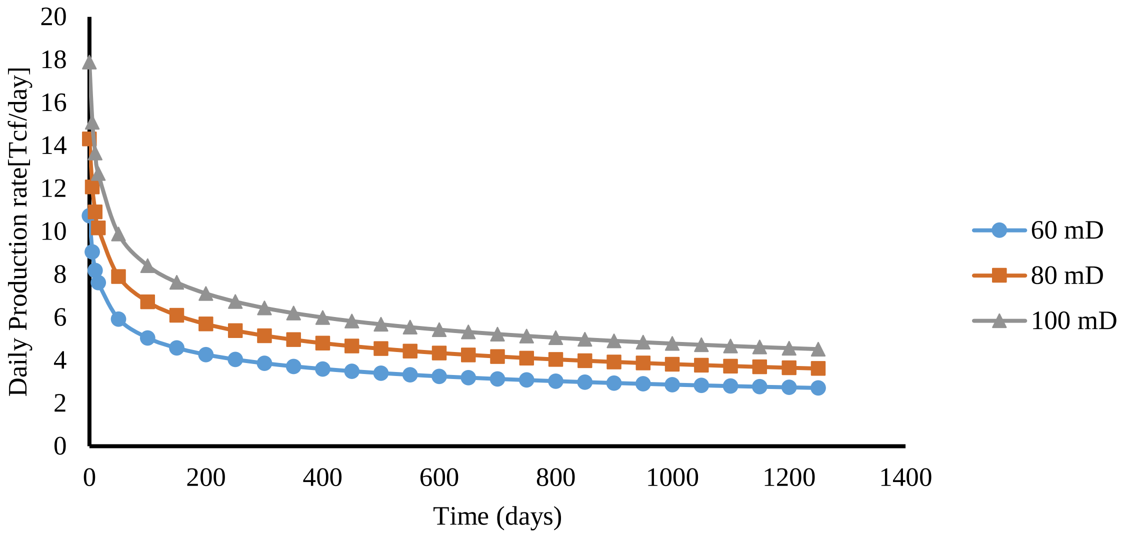

Figure 7.1 Comparison of hydraulic permeability on gas production from the shale reservoir

Figure 7.1 shows that increasing the hydraulic fracture permeability will results in an increase in daily production rate. Figure 7.2 shows the total cumulative gas production and the same relationship as the daily production rate. The relationship is that, increasing hydraulic fracture results in an increase in total cumulative gas production. This is significant because it will be useful to the economy. Meaning that if the demand is high then increase production by increasing the hydraulic fracking permeability.

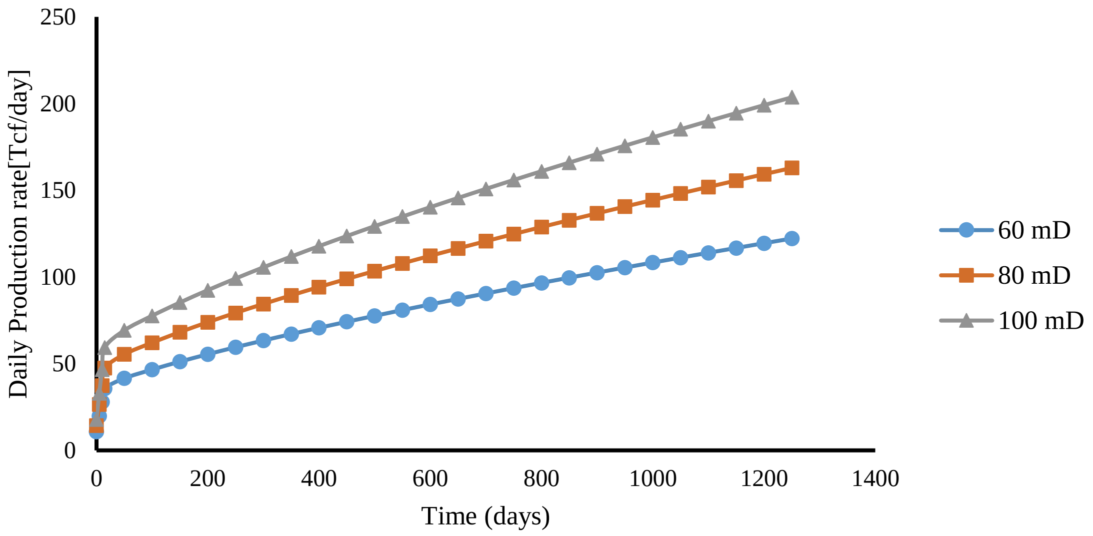

Figure 7.2 Comparison of hydraulic permeability on total cumulative gas production from the shale reservoir

7.2 The effect of changing the drainage radius (r_e) against the production rate.

Drainage radius parameter is varied from 100 m to 300m in the interval of 100m; the effects are shown in Figure 7.3 and 7.4. Increasing drainage radius decreases the production rate (Figure 7.3). In addition, this relationship is also shown in the total cumulative daily production (Figure 7.4). By Figure 7.3, the increase of radius has little significance in the production rate and the cumulative production, hence it can be deduced that drainage radius has little significant in gas production as compared to hydraulic permeability.

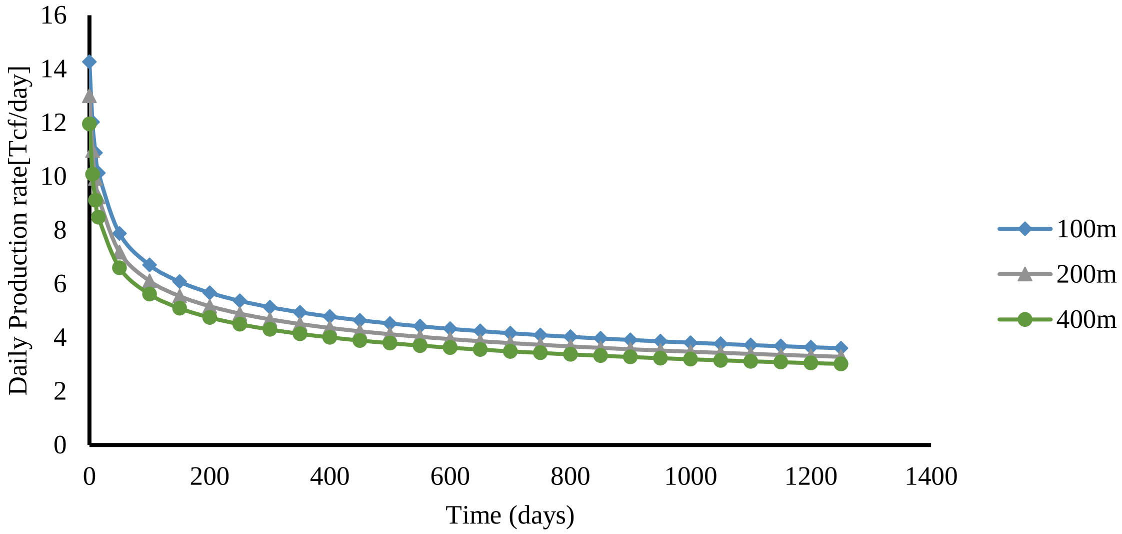

Figure 7.3 Comparison of drainage radius on gas production from the shale reservoir

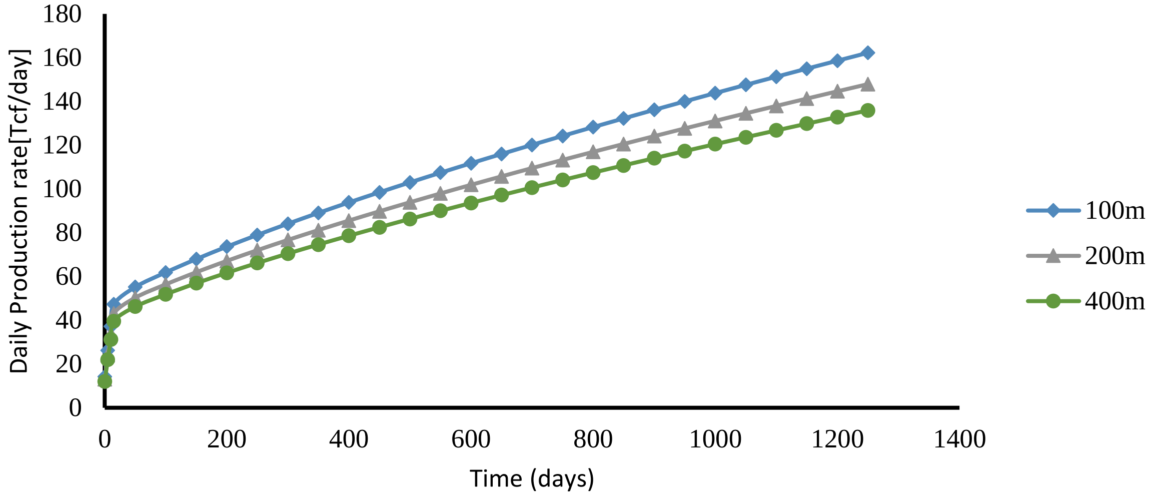

Figure 7.4 Comparison of drainage radius on total cumulative gas production from the shale reservoir

7.3 The effect of changing the initial pressure ($p_m = p_{NF} = p_{HF} = p_i$) against the production rate.

The initial pressure is an extremely important parameter in the reservoir production rate; the reservoir production rate is dependent on this parameter more than the other driving forces. Figure 7.5 and Figure 7.6 shows the graphical mathematical relationship of various rates of gas production against time and the total cumulative gas production rate, respectively. The comparison is made for different initial pressure (s) that are equivalent to 10, 20 and 30 MPa; for both the daily and cumulative production rate. From the curves it can be deducted that initial pressure is very significant in the production rate. From 10 MPa pressure to 20 MPa, there threefold increase in production rate. From 20 to 30 MPa there is approximately two times an increase in production. The relationship between pressure and gas production is directly proportional.

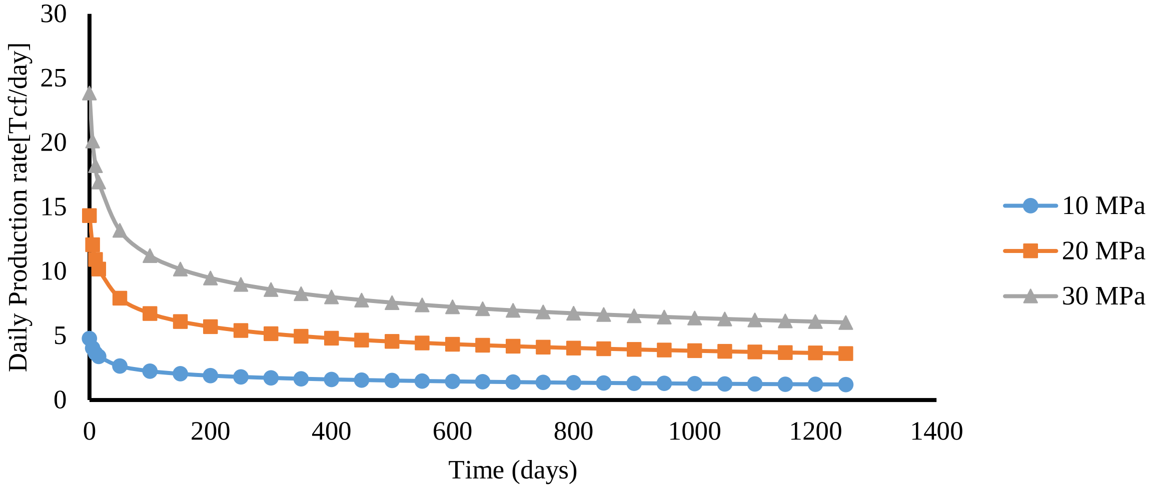

Figure 7.5 Comparison of initial pressure on gas production from the shale gas reservoir

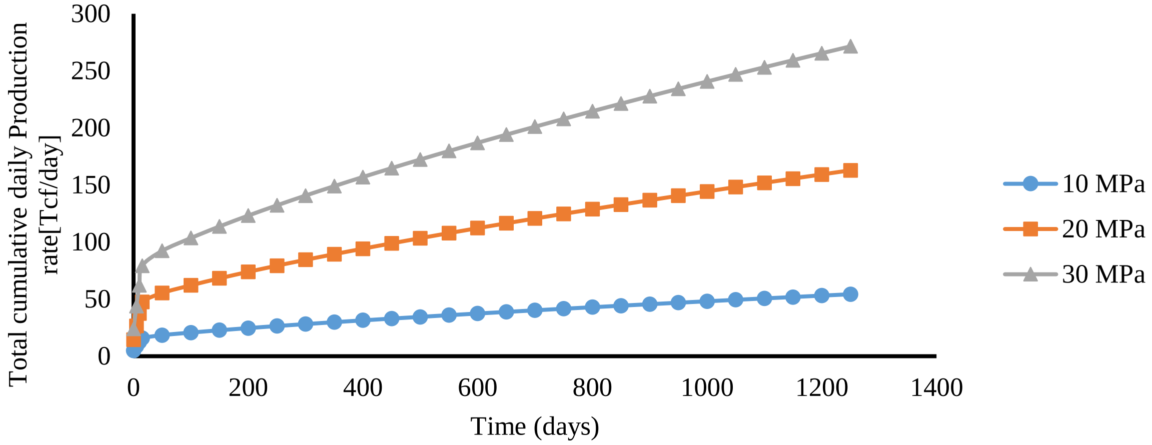

Figure 7.6 Comparison of hydraulic permeability on total cumulative gas production from the shale reservoir

CHAPTER 8 CONCLUSION

In this study the mathematical model for a multi fractured reservoir was established which incorporated adsorption and desorption of shale gas as well as gas slippage flow effect, which were manipulated by using Calculus's rules for differentiation. These rules include the chain rule, the derivative product rule and the derivative quotient rule. The model accounts for the flow in the matrix phase, natural fracturing and hydraulic fracturing. The model had to be developed as a theoretical case due to no official field data for the Karoo basin of South Africa, hence laboratory data will be recommended to fully verify. The main aim was to derive the shale gas mathematical flow model and validate the model. The model was established and validated with the field data from Barnett shale and simulation by (Guo et al., 2018). The model was simulated to test for the three parameters, the permeability hydraulic fracture, the drainage radius and the initial pressure. Therefore, the specific conclusions are as follows in accordance to the objectives:

1. The triple continuum flow model of the shale gas was established by using physical laws: The continuity equation and the Darcy's law. Mathematics which was used is calculus.
2. The model is suitable to be used in any reservoir, following the validation by the Barnett shale and simulation by (Guo et al., 2015).
3. The natural fracture are primary permeable channels for the flows of free gas in shale gas reservoir, hence increasing the permeability of the hydraulic fracture will result in higher production rate of the shale gas. This type of mathematical relation is known to be direct proportionality between hydraulic fracture of permeability and production rate.
4. Drainage radius increases with a decreasing production rate. In the study it can be concluded that the effect of ranging 100m to 300m is insignificant in comparison to

the hydraulic fracture permeability effect on the gas production rate and the total cumulative gas production rate.

5. The initial pressure has greater impact on the production rate of gas compared to the other two parameters (permeability of the hydraulic fracture and the drainage radius). It is also concluded that as the initial pressure increase, the production rate will follow the same trend and increase as well. The same will apply to the total cumulative gas production.

References

Abdussah, D., & Ershaghi, I., 1986. Triple-porosity systems for representing naturally fractured reservoirs. *Society of Petroleum Engineers,* 1(2). pp. 113-127.

Ahmed, T., 2001. *Reservoir engineering handbook.* 2nd ed. Woburn, USA: Gulf Professional Publishing.

Al-Ahmadi, A. & Ershaghi, I., 1996. Pressure transient analysis of dually fractured reservoirs. *Society of Petroleum Engineers,* 1(1), pp. 93-100.

Anon., 2018. *Esircworldwide.* [Online]
Available at: https://i1.wp.com/esircworldwide.com/wp-content/uploads/1-esirc-world-wide-Fracking-History-HORIZONTAL-WELLS.jpg?resize=604%2C254&ssl=1
[Accessed 30 January 2018].

Barenblatt, G. I., Zhelto, I. P. & Kochina, I. N., 1960. Basic concepts of the theory of seepage of homogeneous liquids in fissured rocks. *Journal of Applied Mathematical Mechanics,* 24(5), pp. 852-864.

Basniev, K. S., Dmitriev, N. M. & Chilingar, G. V., 2012. *Mechanics of fluid flow.* 1st ed. Beverly: Scivener Publishing.

Belyadi, H., Fathi, E. & Belyadi, F., 2017. *Hydraulic fracturing in unconventional reservoirs: Theories, operations, and economics analysis.* 1st ed. Oxford: Gulf Professional Publishing.

Bo, P., Xueyong, F., Xunjie, W. & Wenying, L., 2017. Key steps of carbon emission and low carbon measures in the constrution of bituminous pavement. *International Journal of Pavement Research and Technology,* vol.10(no.1), p. 476–487.

Burwen, J. & Flegal, J., 2013. *Unconventional gas exploration and production.* [Online]
Available at: http://americanenergyinnovation.org/wp-content/uploads/2013/03/Case-Unconventional-Gas.pdf
[Accessed 1 August 2018].

Bustin, A., Bustin, R. & Cui, X., 2008. *Importance of fabric on the production of gas shales..* Presented at unconventional reservoir conference in Colorado USA, Society of Petroleum Engineers.

Campbell, S. A., Mielke, P. & Götz, A. E., 2016. Geothermal energy from the Main Karoo Basin? New insights from borehole KWV-1 (Eastern Cape, South Africa). *Geothermal Energy,* 4(1), pp. 1-19.

Chaoa, L. et al., 2016. Analysis on effective reservoirs and length optimization of horizontal wells in the Sulige Gasfield. *Natural Gas Industry B 3,* 3(3), pp. 245-252.

Cinco-Ley, H. & Samaniego-V., F., 1981. Transient pressure analysis for fractured wells. *Journal of Petroleum Technology,* 33(9), pp. 1749 - 1766.

Cooper, J. r., Stamford, L. & Azapagic, A., 2016. Shale Gas: A Review of the Economic, Environmental, and Social Sustainability. *Energy Technology,* 4(7), pp. 772-792.

Correa, G., Felipe, T., Osorio, N. & Restrepo Restrepo, D. P., 2009. *Unconventional Natural Gas Resevoirs.* [Online]
Available at: http://www.redalyc.org/html/1470/147012859006/
[Accessed 23 March 2018].

Crain, E. R., 2006. *Crain's petrophysical handbook.* [Online]
Available at: https://www.spec2000.net/
[Accessed 28 March 2018].

Dake, L. P., 1978. *Fundamentals of reservoir engineering.* 1st ed. Amsterdam: Elsevier Science B.V..

Da-yu, Z. et al., 2015. *Theoretical gas phase compressibility factor of mixed refrigerants in auto-cascade refrigeration system.* Heilongjiang Province, Atlantis Press.

De Kock, M. O. et al., 2017. Deflating the shale gas potential of South Africa's Main Karoo basin. *South African Journal of Science,* 113(9), pp. 1-12.

De Wit, M. J., 2011. The great shale debate in the Karoo. *South African Journal of Science,* 107(7/8), pp. 1-7.

Degenhardt, R., 2011. *EPA Investigates Fracking Impacts - EHS Journal.* [Online]
Available at: http://ehsjournal.org/http:/ehsjournal.org/rachel-degenhardt/epa-investigates-fracking-impacts-hydraulic-fracturing/2011/
[Accessed 29 March 2018].

Geel, C. et al., 2013. Shale gas characteristics of Perminian black shale in South Afric: results from recent drilling in the Ecca Group (Eastern Cape). *Energy Procedia,* 40(1), pp. 256-265.

Grieser, W. V., Shelley, R. F. & Soliman, M. Y., 2009. *Predicting production outcome from multi-stage, horizontal Barnett completions..* Oklahoma City, Society of Petroleum Engineers, pp. 1-10.

Gholami, M and Talaie, M. R., 2010. Investigation of simplifying assumptions in mathematical modeling of natural gas dehydration using adsorption process and introduction of a new accurate LDF model. *Industrial & Engineering Chemistry Research,* 49(2), pp. 838-846.

Guarnone, M. et al., 2012. An unconventional mindset for shale gas surface facilities. *Journal of Natural Gas Science and Engineering,* 6(1), pp. 14-23.

Guo, C., Wei, M. & Liu, H., 2015. Modeling gas production from shale reservoirs considering multiple transport mechanisms. *Plos One,* 10(12), pp. 1-24.

Guo, C., Wei, M. & Liu, H., 2018. Study of gas production from shale reservoirs with multi-stage hydraulic fracturing horizontal well considering multiple transport mechanisms. *PLos One,* 13(1), pp. 1-21.

Haghshenas, B., Clarkson, R. & Chen, S., 2013. *Multi-porosity, multi-permeability models for shale gas reservoirs.* Alberta Canada, SPE Unconvetional Resources Conference and Exhibition.

Hao, Y. et al., 2017. Shale gas simulation considering natural fracture, gas desorption, and slippage flow effects using conventional modified model. *J Petrl Explor Prod Technol,* 8(2), pp. 607-615.

Johnson, M. R. et al., 1996. Stratigraphy of the Karoo Supergroup in the Southern Africa: an overview. *Journal of African Earth Sciences,* 23(1), pp. 3-15.

Kudapa, V. K., Sharma, P., Kunal, V. & Gupta, D. K., 2017. Modeling and simulation of gas flow behavior in shale reservoirs. *Journal of Petroleum Exploration and Production Technology,* 7(4), pp. 1095-1112.

Lu, X. C., Li, F. C. & Watson, A. T., 1995. Adsorption studies of natural gas storage in devonian shales. *Society of Petroleum Engineers,* 10(2), pp. 109-113.

Renyi, C., Linsong, C. & Peiqing, L., 2017. MathematicalmModel of Shale Gas Reservoirs coupled by desorption, stress sensitivity and Fracture Finite Conductivity. *Physical and Numerical Simulation of Geotechnical Engineering,* 10(2), pp. 27-30.

Saliem, F., 2015. *Framework to assess the economic reality of shale gas in South Africa.* [Online]
Available at: https://www.agrisa.co.za/wp-content/uploads/2015/02/framing_the_economics_of_shale_gas_in_south_africa__report_web.pdf
[Accessed 20 January 2018].

SAMSA, 2011. *Offshore oil and gas – Industry profile. Annual Report on policy and regulation,* Pretoria South Africa: SAMSA Centre for policy and regulation.

Santillán, D., Juanes, R. & Cueto-Felgueroso, L., 2018. Phase Field Model of Hydraulic Fracturing in Poroelastic Media: Fracture Propagation, Arrest, and Branching Under Fluid Injection and Extraction. *Journal of Geophysical,* 123(3), pp. 2127-2155.

Shusheng, G. et al., 2017. A coupling model for gas diffusion and seepage in SRV section of shale gas reservoirs. *Natural gas industry B,* 4(2), pp. 120-126.

Speight, J., 2008. *Synthetic Fuels Properties: Properties, Process and Performance.* 1st ed. New York: The McGraw-Hil.

Tan, L., Zuo, L. & Wang, B., 2018. Methods of Decline Curve Analysis for Shale Gas Reservoirs. *Energies: International Journal of Coal Geology,* 11(3), pp. 1-13.

Viljoen, J. H. A., 1994. Sedimentology of the Collingham Formation, Karoo Supergroup. *South African Journal of Geology,* 97(2), pp. 167-183.

Wang, W., Yao, J., Sun, H. & Song, W., 2015. Influence of gas transport mechanism on the productivity of multi-stage fractured horizontal wells in shale gas reservoirs. *Petroleum Science,* 12(4), pp. 664-673.

Warren, J. E. & Root, P. J., 1963. The Behavior of Naturally Fractured Reservoirs. *Society of Petroleum Engineers Journal,* 3(3), pp. 245-255.

Weast, R. C., 1984. *CRC Handbook of Chemistry and Physics.* 65th ed. Boca Raton, Florida. USA.: CRC Press, Inc.

Welty, J. R., Wicks, C. E., Wilson, R. E. & Rorrer, G. L., 2008. *Fundamentals of Momentum, Heat, and Mass Transfer.* 5th ed. Danvers: John Wiley & Sons.

Wu, Y.-S., Kang, Z. & Zhang, W., 2009. *A triple-continuum model for production in tight fractured reservoirs.* Texas, USA, Paper SPE 118944 presented at the SPE Hydraulic Fracturing Technology Conference.

Yao, J., Sun, H. & Huang, Z., 2013. Key mechanical problems in the development of shale gas reservoirs. *Scientia sinica physica mechanica and astronomica,* 43(12), pp. 1527-1547.

Zeng, Z. & Grigg, R., 2006. A Criterion for Non-Darcy Flow in Porous Media. *Springer,* 63(1), pp. 57-69.

Zhang, W., Xu, J. & Jiang, R., 2016. Production forecast of fractured shale gas reservoir considering multi-scale gas flow. *Journal of Petroleum Exploration and Production Technology,* 7(4), p. 1071–1083.

Zhang, W. et al., 2017. Employing a quad-porosity numericalmodel to analyze the productivity of shale gas reservoir. *Journal of Petroleum Science and Engineering,* 63(1), pp. 1046-1055.

Appendices

Appendix A

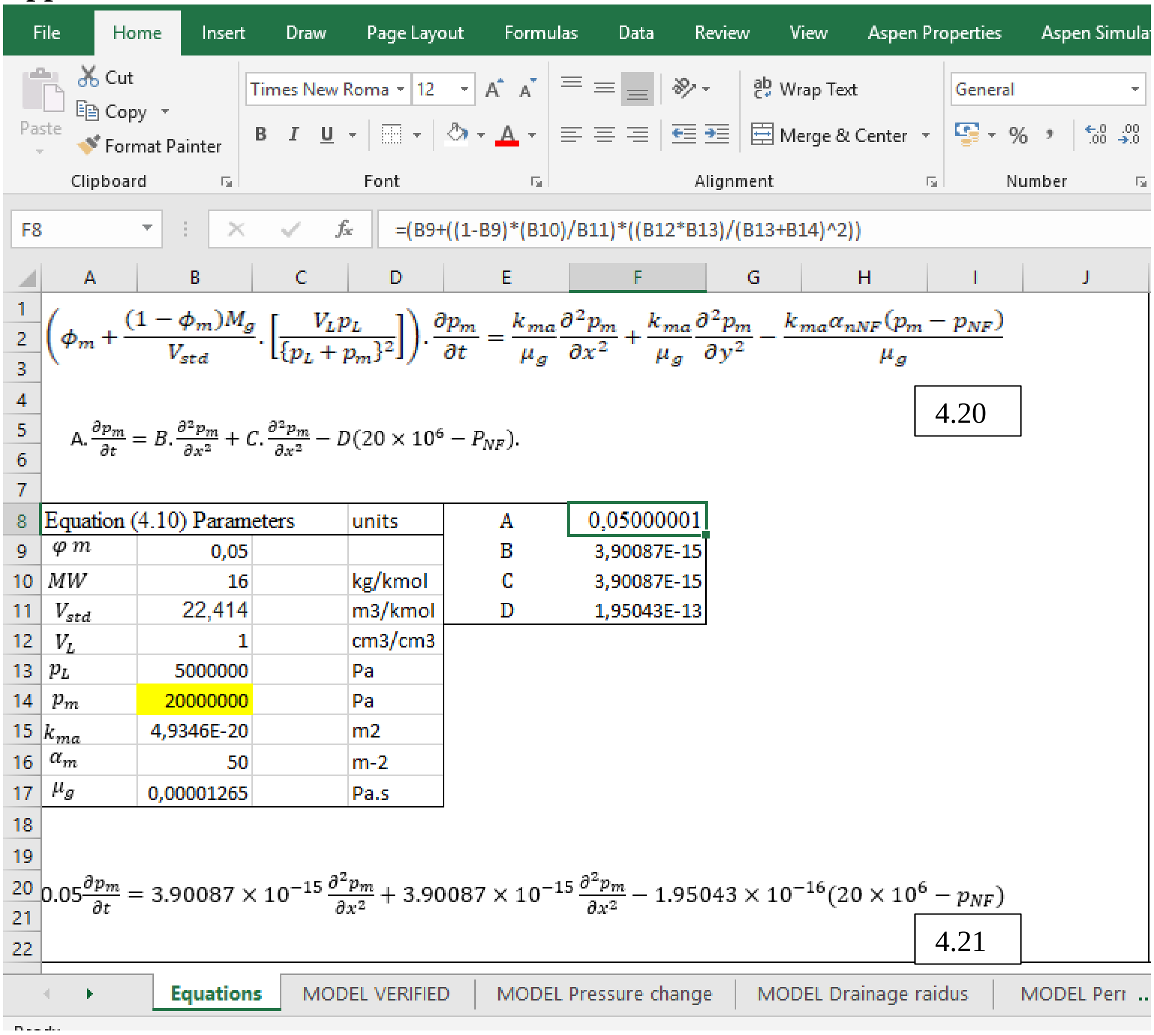

Figure A.1 derivation of the general equation of the matrix phase

After deriving the general equation (4.20) of the matrix phase, the equation was further simplified by putting capital letters A, B, C and D to denote the parameters. (Equation (4.20) Parameters). To determine A, B, C and D the following calculation is performed in excel spread sheet by substituting data from (Guo et al., 2015).

A= $\left(\phi_m + \frac{(1-\phi_m)M_g}{V_{std}}.\left[\frac{V_L p_L}{\{p_L+p_m\}^2}\right]\right)$= (B9+((1-B9)*(B10)/B11)*((B12*B13)/(B13+B14)^2))=0.05

B = $\frac{k_{ma}}{\mu_g}$ = B15/B17=3.9X10^{-15}

C = $\frac{k_{ma}}{\mu_g}$ = B15/B17 = 3.9X10^{-15}

D = $\frac{k_{ma}\alpha_{m\to NF}}{\mu_g}$ = (B15*B16)/B17=1.95X10^{-16}.

Then equation (4.21) is determined.

$$0.05\frac{\partial p_m}{\partial t} = 3.90087\times10^{-15}\frac{\partial^2 p_m}{\partial x^2} + 3.90087\times10^{-15}\frac{\partial^2 p_m}{\partial x^2} - 1.95043\times10^{-16}(20\times10^6 - p_{NF}) \quad (4.21)$$

Appendix B

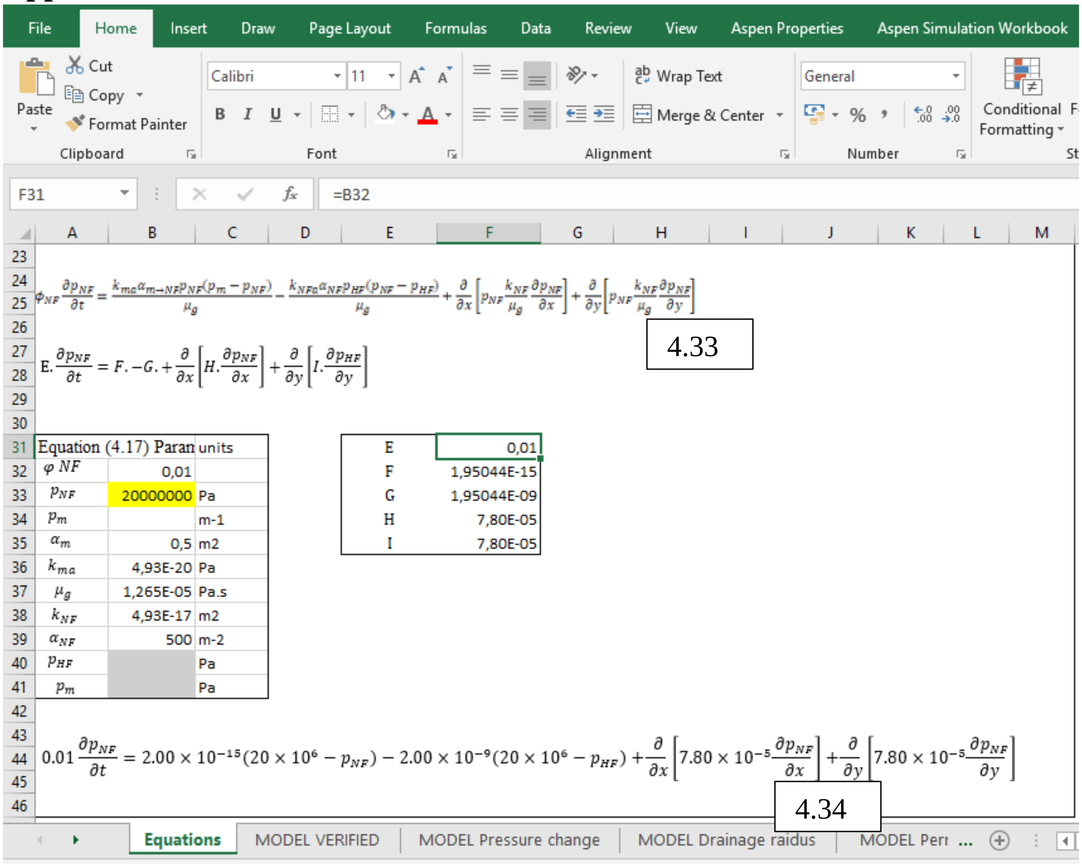

Figure B.1 derivation of the general equation of the natural fracture phase

After deriving the general equation (equation 4.33) of the natural fracture phase, the same procedure is followed as in Appendix A. Capital letters E, F, G, H and I is denoted to the parameters (Equation 4.33 Parameters). To determine E, F, G, H and I the following calculation is performed in excel spread sheet by substituting data from (Guo et al., 2015).

E = ϕ_{NF} =B32 =0.01

F = $\frac{k_{ma}\alpha_{m\to NF}p_{NF}(p_m - p_{NF})}{\mu_g}$ = (B36*B35)/B37= 1.95X10^{-15}

G = $\frac{k_{NFa}\alpha_{NF\to HF}p_{HF}(p_{NF} - p_{HF})}{\mu_g}$ = (B38*B39)/B37= 1.95X10^{-9}

H = $p_{NF}\frac{k_{NF}}{\mu_g}$ = B33*(B38/B37) = 7.8 x 10^{-5}

I = $p_{NF}\frac{k_{NF}}{\mu_g}$ = B33*(B38/B37) = 7.8 x 10^{-5}

Then equation (4.32) is determined.

$$0.01\frac{\partial p_{NF}}{\partial t} = 2.00\times10^{-15}(20\times10^{6} - p_{NF}) - 2.00\times10^{-9}(20\times10^{6} - p_{HF}) + \frac{\partial}{\partial x}\left[7.80\times10^{-5}\frac{\partial p_{NF}}{\partial x}\right] + \frac{\partial}{\partial y}\left[7.80\times10^{-5}\frac{\partial p_{NF}}{\partial y}\right] \qquad (4.34)$$

Appendix C

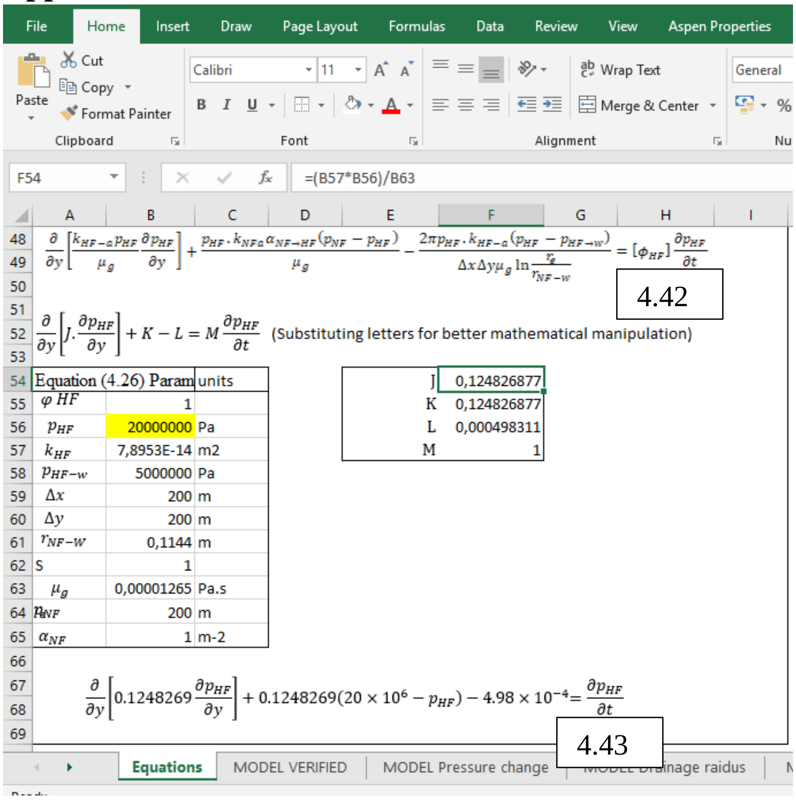

Figure C.1 derivation of the general equation of the hydraulic fracture phase

After deriving the general equation (equation 4.42) of the hydraulic fracture phase, same procedure is followed as in Appendix A. Capital letters J, K, L and M is denoted to the parameters (Equation 4.42 Parameters). To determine J, K, L and M the following calculation is performed in excel spread sheet by substituting data from (Guo et al., 2015).

J = $\frac{k_{HF-a} p_{HF}}{\mu_g}$= (B57*B56)/B63 = 0,124826877

K = $\frac{p_{HF}.k_{NFa}\alpha_{NF\rightarrow HF}(p_{NF}-p_{HF})}{\mu_g}$ = ((B56*B57*B65))/B63= 0,124826877

L $\frac{2\pi p_{HF}.k_{HF-a}(p_{HF}-p_{HF\rightarrow w})}{\Delta x \Delta y \mu_g \ln\frac{r_e}{r_{NF-w}}}$= (2*PI()*B57*B56)*(B56-B58)/(B59*B60*LN(B64/B61))= 0,000498311

M = ϕ_{HF}= B55 = 1

Then equation (4.43) is determined.

$$\frac{\partial}{\partial y}\left[0.1248269\frac{\partial p_{HF}}{\partial y}\right] + 0.1248269(20\times 10^6 - p_{HF}) - 4.98\times 10^{-4} = \frac{\partial p_{HF}}{\partial t} \qquad (4.43)$$

Appendix D

Hydraulic Fracture

```
% Matlab Program 5: Diffusion in one dimensional Stimulated Gas Reservoir
%within the
% Explicit Method
clear;

% Parameters to define the HYDRAULIC FRACTURE PHASE’s equation and the
range in space and time
L = 1300.; % Length of the Stimulated Gas Reservoir (SGR) (m)
T =1300; % Final time (days)
%%%%%%%%%%%%%%%%%%%%%%%%%%%%%%%%%%%%%%%%%%%%%%%%%%%%%%%%%%%%%%%%%%%%%%%%%%%%

% Parameters needed to solve the equation within the explicit method
timek = 2500; % Number of time steps
dt = T/timek;
nn = 50; % Number of space steps
dx = L/nn;
cond = 1/4; % Conductivity
b = 0.1248669; % Stability parameter (b=<1)
%%%%%%%%%%%%%%%%%%%%%%%%%%%%%%%%%%%%%%%%%%%%%%%%%%%%%%%%%%%%%%%%%%%%%%%%%%%%


% Initial pressure of the SGR: a sinus.
for i = 1:nn+1
x(i) =(i-1)*dx;
p(i,1) =sin(pi*x(i));
end
% Pressure at the boundary (P=0)
for k=1:timek
p(1,k) = 0.;
p(nn+1,k) = 0.;
time(k) = (k-1)*dt;
end
%%%%%%%%%%%%%%%%%%%%%%%%%%%%%%%%%%%%%%%%%%%%%%%%%%%%%%%%%%%%%%%%%%%%%%%%%%%%


% Implementation of the explicit method
for k=1:timek % Time Loop
for i=2:nn; %   Space Loop
p(i,k+1) =p(i,k) + b*(p(i-1,k)+p(i+1,k)-2.*p(i,k))+dt*(0.1248269*(20*10^6-
p(i,k))-4.98*10^(-4));
end
end
%%%%%%%%%%%%%%%%%%%%%%%%%%%%%%%%%%%%%%%%%%%%%%%%%%%%%%%%%%%%%%%%%%%%%%%%%%%%


% Graphical representation of the pressure
figure(1)
plot(x,p(:,1),'-',x,p(:,500),'-',x,p(:,800),'-',x,p(:,1200),'-')
title('Pressure behaviour)
xlabel('y(m)')
ylabel('Pressure(Pa)')
```

Appendix E

Natural fracture

```
%  This is Diffusion in 2D space for the Stimulated Gas Reservoir.
%  The explicit finite difference method is used for Natural Fracture Phase
%%%%%%%%%%%%%%%%%%%%%%%%%%%%%%%%%%%%%%%%%%%%%%%%%%%%%%%%%%%%%%%%%%%%%%%%%%%%

clear;
L = 1300;     % length in the x-direction (m)
W = 600;      % length in the y-direction
Tend = 1300.;% final time (Days)
maxk = 2500;
dt = Tend/maxk;
n = 50.;      % Number of space steps

%%%%%%%%%%%%%%%%%%%%%%%%%%%%%%%%%%%%%%%%%%%%%%%%%%%%%%%%%%%%%%%%%%%%%%%%%%%%

% initial condition and part of boundary condition
u(1:n+1,1:n+1,1:maxk+1) = 20*10^6.;
dx = L/n;
dy = W/n;   % use dx = dy = h
h = dx;
b = dt/(h*h);
cond = .002;    % Coefficient of the partial derivative function
spheat = 1.0;   % Constant
rho = 1.;   % density
a = cond/(spheat*rho);
alpha = a*b;
c = 7.8*10^(-5);
for i = 1:n+1
   x(i) =(i-1)*h;   % use dx = dy = h
   y(i) =(i-1)*h;
end
%%%%%%%%%%%%%%%%%%%%%%%%%%%%%%%%%%%%%%%%%%%%%%%%%%%%%%%%%%%%%%%%%%%%%%%%%%%%

% boundary condition
for k=1:maxk+1
   time(k) = (k-1)*dt;
   for j=1:n+1
      u(1,j,k) =300.*(k<120)+ 70.;
   end
end
%%%%%%%%%%%%%%%%%%%%%%%%%%%%%%%%%%%%%%%%%%%%%%%%%%%%%%%%%%%%%%%%%%%%%%%%%%%%

%   Explicit finite difference method computation
for k=1:maxk
   for j = 2:n
      for i = 2:n
         u(i,j,k+1)= alpha*(u(i-1,j,k)+u(i+1,j,k)+u(i,j-1,k)+u(i,j+1,k));
      end
   end
end
% Pressure versus space at the final time
mesh(x,y,u(:,:,maxk)')
title('Pressure within the explicit method')
xlabel('y(m)')
zlabel('Pressure(Pa)')
```

Appendix F

Matrix Phase

```
%  This is diffusion in 2D space (Matrix Phase).
%  The explicit finite difference method is used for the Matrix phase the
behaviour is expected to be the same as natural fracture since they are
both in 2 D space.
%%%%%%%%%%%%%%%%%%%%%%%%%%%%%%%%%%%%%%%%%%%%%%%%%%%%%%%%%%%%%%%%%%%%%%%%%%%%

clear;
L = 1300;     % length in the x-direction (m)
W = 600;      % length in the y-direction (m)
Tend = 1300.;% final time (Days)
maxk = 2500;
dt = Tend/maxk;
n = 50.;      % Number of space steps

%%%%%%%%%%%%%%%%%%%%%%%%%%%%%%%%%%%%%%%%%%%%%%%%%%%%%%%%%%%%%%%%%%%%%%%%%%%%

% initial condition and part of boundary condition
u(1:n+1,1:n+1,1:maxk+1) = 20*10^6.;
dx = L/n;
dy = W/n;    % use dx = dy = h
h = dx;
b = dt/(h*h);
cond = 3.9*10(-15);     % thermal conductivity
spheat = 1.0;    % specific heat
rho = 1.;    % density
a = cond/(spheat*rho);
alpha = a*b;
c = 7.8*10^(-5);
for i = 1:n+1
   x(i) =(i-1)*h;    % use dx = dy = h
   y(i) =(i-1)*h;
end
%%%%%%%%%%%%%%%%%%%%%%%%%%%%%%%%%%%%%%%%%%%%%%%%%%%%%%%%%%%%%%%%%%%%%%%%%%%%

% boundary condition
for k=1:maxk+1
   time(k) = (k-1)*dt;
   for j=1:n+1
      u(1,j,k) =300.*(k<120)+ 70.;
   end
end
%%%%%%%%%%%%%%%%%%%%%%%%%%%%%%%%%%%%%%%%%%%%%%%%%%%%%%%%%%%%%%%%%%%%%%%%%%%%

%   finite difference method computation
for k=1:maxk
   for j = 2:n
      for i = 2:n
         u(i,j,k+1)= alpha*(u(i-1,j,k)+u(i+1,j,k)+u(i,j-1,k)+u(i,j+1,k));

      end
   end
end

% temperature versus space at the final time
mesh(x,y,u(:,:,maxk)')
```

```
figure(3)
mesh(x,time,p')
title('Pressure within the explicit method')
xlabel('y(m)')
ylabel('pressure(Pa)')
```

Appendix G

Table G.1: Model and field data comparison

t(day)	Field Data	Model
0	0	4.58
5	4.76	3.86
8.5	3.45	3.7
10	3.2	3.5
15	3.3	3.25
25	3.78	3.24
25	3.56	3.05
50	3.2	2.53
90	2.7	2.19
100	2.27	2.14
100	2.8	2.15
125	2.85	2
150	2.78	1.95
180	2.5	1.86
192	1.56	1.84
200	2.5	1.82
250	2.24	1.72
300	2.2	1.65
350	2	1.59
360	2	0
365	2.05	0
380	1	0
400	1.98	1.54
403	0.907	0
404	1.5	0
405	1.24	0
415	1.91	0
450	1.8	1.49
467	1.5	0
475	1.53	0
500	1.9	1.45
500	1.9	1.45
550	1.78	1.42
600	1.7	1.39
650	1.75	1.36
670	1	0
700	1.53	1.34
750	1.33	1.32
800	1.4	1.29
850	1.35	1.27
900	1.2	1.26
950	1.16	1.24
1000	1.18	1.22
1010	1	0
1050	1	1.21
1100	1.189	1.2
1150	0	1.18
1200	0	1.17
1250	0	1.16

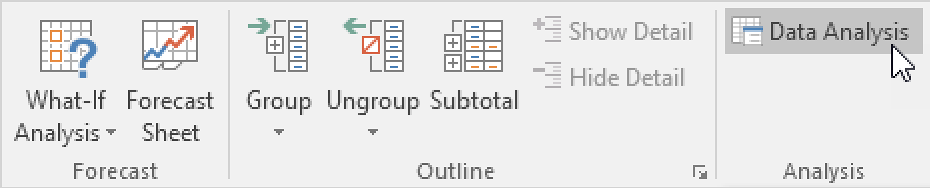

T-test

1. Data Analysis tab was tabbed to releases option of the test.

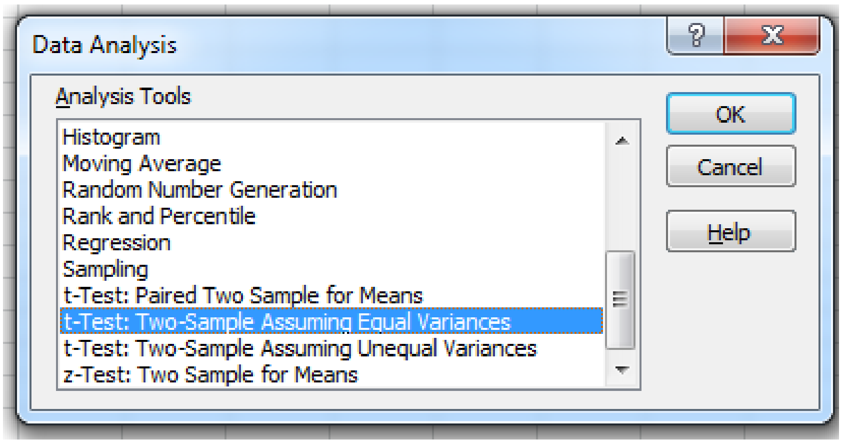

2. 't-test: Two-Sample Assuming Equal Variances' was selected

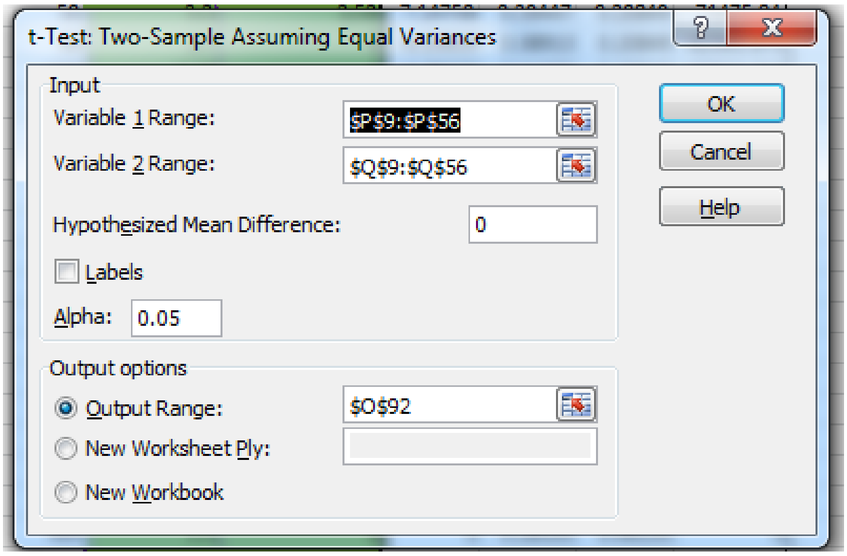

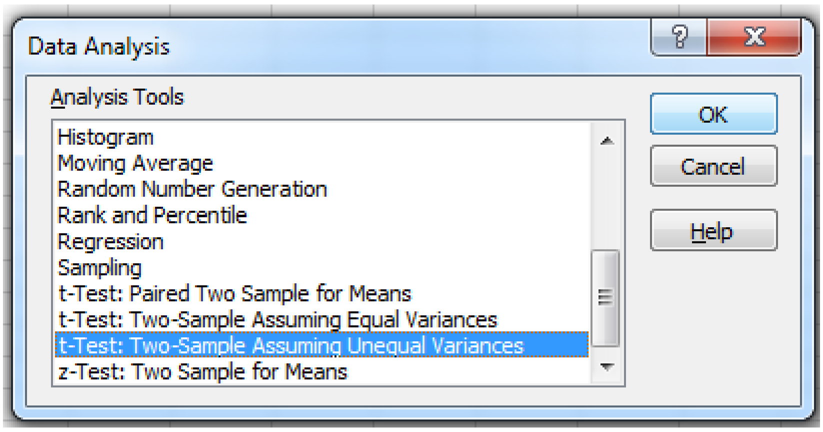

Data in Table G.1 was selected 'Field Data' was put into 'Variable 1 Range' tab and model was put into 'Variable 2 Range:' 'Hypothesized Mean Difference:' was set to 0. 'Output Range:' was selected to be on grid O92. T test: t-test: Paired Two Sample for Means table is generated

t-Test: Two-Sample Assuming Unequal Variances

	Variable 1	*Variable 2*
Mean	1.865333333	1.502708333
Variance	1.047440099	1.304007402
Observations	48	48
Hypothesized Mean Difference	0	
df	93	
t Stat	1.638365208	
P(T<=t) one-tail	0.052362288	
t Critical one-tail	1.661403674	
P(T<=t) two-tail	0.104724576	
t Critical two-tail	1.985801814	

Two-tail test (inequality) was performed. lf t Stat < -t Critical two-tail or t Stat > t Critical two-tail, therefore the null hypothesis is rejected. This is not the case, -1.985< 1.638< 1.985. Therefore, the null hypothesis is not rejected. The observed difference between the samples means (1.865 - 1.503) does have enough evidence that the average production rate between field data and model data differ significantly.